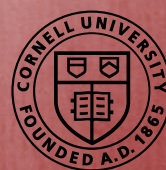# REU PROGRAM IN INTERDISCIPLINARY MATERIALS RESEARCH

Research Reports by Students supported by Cornell Center for Materials Research (NSF MRSEC Program, DMR-1719875).

TABLE OF CONTENTS

Student

Faculty Advisor

- Prof. Dan Ralph
- Prof. Itai Cohen
- Prof. Margaret Frey
- Prof. Christopher Ober
- Prof. Nandini Ananth
- Prof. Jeevak Parpia
- Prof. Brad Ramshaw

Spin-Torque Transfer Magnetic Random Access Memory Utilizing Films with Perpendicular Magnetic Anisotropy

Aaron Coe[1,2], Jonathan Gibbons[2], Arnab Bose[2], and Dan Ralph[2]

[1]Bethel University, Saint Paul, Minnesota

[2]Cornell Center for Materials Research, Cornell University, Ithaca, New York

(Dated: August 8, 2018)

A magnet with the characteristic of perpendicular magnetic anisotropy (PMA) or out-of-plane magnetization will enable desirable thermal stability for STT-MRAM cells at a scale below 50 nm. This research investigated growing ferromagnetic materials with PMA using disprosium, cobalt, magnesium oxygen and iron-cobalt-boron, utilizing DC magnetron sputtering. The resulting samples did display PMA. However, the PMA was weaker than reported by other groups. Additionally, MgN was explored to determine if its peculiar magnetic ordering produces nonstandard torques and was found to produce standard torques at room temperature.

I. INTRODUCTION

Modern computers use a hierarchy of memory types for storing data long term and for active use. Because different memory types provide different advantages, the use of multiple types of memory in a single computer is needed. Random Access Memory (RAM) is used by the computer to store data that it accesses constantly. When a program is run, the information related to that program is stored in the computer's RAM. If this data was stored in main memory (hard drive disks, solid state drives, etc), the computer would not be able to access the data as quickly and programs would run a few order of magnitudes slower. Instead main memory functions as a storage place to store data long term (saving files) and to store any data that cannot fit in RAM. The memory types used in RAM also cannot be used effectively in main memory without a significant increase in energy usage, cost, and risk if the computer loses power. The memory types used in RAM are volatile they require constant refreshing to keep memory and they lose all data when the power is lost [1]. These memory types are more expensive than hard drive storage. To make a 1 Terabyte (TB) main memory storage out of RAM memory types would cost over $10,000.

Spin-Torque Transfer Magnetic Random Access Memory (STT-MRAM) may provide the capability for read and write times comparable to dynamic random-access memory (DRAM) and static random-access memory (SRAM), common memory types used in RAM, while providing the non-volatility of a hard drive [2]. If RAM is replaced with STT-MRAM, a computer could be powered off with programs running and save that state. Then when the computer is powered on, it will boot up with those programs running. There would be no need to start up the operating system, except for freeing dynamically allocated memory, making boot times faster than computers with Solid State Drives (SSDs). If main memory were replaced with STT-MRAM, the cost of a program reading or writing to main memory could be reduced by a few orders of magnitude. Programs would be able to run faster and work with more data in this case.

MRAM uses a ferromagnetic layer, known as the free layer, to store the memory bit. The direction of the magnetization of this layer determines whether the bit is a one or a zero. Initially, magnetic switching of the free layer was done by applying an external magnetic field by flowing current through wires to induce a field. However, when the system was scaled down, the current requirements became too large and the external field was found to affect bits other than the one meant to be switched [3, 4].

Spin-torque transfer (STT) is another technique used for switching the direction of the free layer. This method does not suffer from the same problems as external field switching such as power and scaling. Spin-torque transfer utilizes the spin of electrons and the properties of ferromagnetic materials to create torques that cause the magnet to precess and eventually flip magnetization directions [3–5]. Currently, EVERSPIN Technologies sells STT-MRAM based memory up to 256 Mb as an alternative RAM memory type. They claim their units are comparable to DRAM which has access times around 10 ns (extremely fast compared to hard drive disk access time of a few miliseconds) [2]. STT-MRAM is still in its infancy commercially and the size of a bit will need to be scaled down before it can truly compete with other memory types. Unfortunately, thermal energy becomes a problem for most STT-MRAM designs when bit sizes fall below 50 nm [3, 4]. The following investigation explores using ferromagnetic layers with out-of-plane magnetization for a new generation of STT-MRAM.

II. SPIN-TORQUE TRANSFER MAGNETIC RANDOM ACCESS MEMORY

Electron spin is an intrinsic property of electrons. While the electron does not actually spin (being a point particle), it does carry angular momentum. Ferromagnetic materials contain a net spin polarization. Therefore, there is a net direction for the electrons' spin which means that there is a net field generated by their spinning, giving rise to a net field in ferromagnetic materials.

Ferromagnetic materials prefer to keep their net spin, which means when a current of non-spin polarized electrons flow through a ferromagnet, the spin direction of the electrons will be reoriented to align with the field of the ferromagnet. But if the spin direction of electrons is being changed, then the angular momentum must go somewhere which happens to be into the magnetization. The magnetization will apply a torque on the electrons and the electrons will apply a torque on the magnetization [5]. For charge currents, there is no change in the magnetization direction but for a spin polarized current, there is a net torque on the magnetization which can cause it to change direction.

STT-MRAM utilizes magnetic tunnel junctions (MTJs) shown in Fig 1. The fixed layer is used to generate the spin current (a spin polarized charge current in this case but it can also be purely spin current with no net charge movement). A spin current can be generated by flowing charge current through the fixed layer and into the free layer. The fixed layer will act as a filter for the spin of the electrons creating a net spin and therefore a spin current which flows into the free layer [3, 6]. However, this technique creates heat through joule heating and at maximum efficiency of momentum transfer between spin and magnetization is limited. This is because a single electron carries a single electron's worth of charge and angular momentum so the greatest ratio between momentum imparted and the charge of the electron is $\frac{\hbar}{2e}$
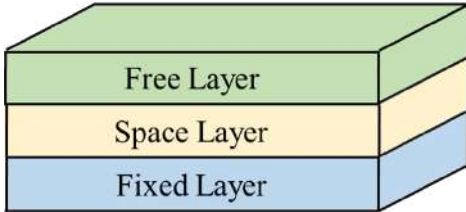

FIG. 1. The free layer is where the bit state of a 1 or 0 is stored. The spacer layer acts as a barrier to keep the fixed layer and free layer from magnetically coupling (one layer cannot be flipped without flipping the other layer) and allows for tunneling between the fixed layer and free layer. Additionally, the fixed layer is used to generate the desired spin current for switching and reading the state of the free layer.

Another method for generating spin current is through the spin Hall effect (SHE). When charge current flows through a conductive material with large spin-orbit coupling, pure spin current will start to flow in a direction perpendicular to both the charge current and the spin direction (Fig 2) [7, 8]. For a non-spin polarized charge current, half the electrons with spin in-plane but perpendicular to the direction of the charge current, will flow upwards out of the film toward the free layer for a non-ferromagnetic conductive material. Limitations on the use of the SHE include that it is observable only in materials with large spin-orbit coupling and the size of the spin current generated through the effect is small

[6]. For magnetic switching, SHE's advantages outweigh its disadvantages because it is not limited by the ratio mentioned earlier and it is used in this investigation for analyzing material properties.
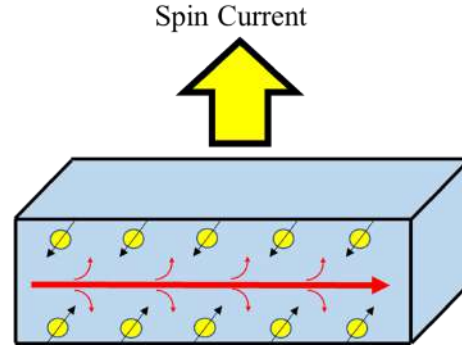

FIG. 2. Illustration of spin current generation through the SHE. As current flows to the right, in the plane of the page, electrons with spins in and out of the page flow downwards and upwards respectively.

When charge current is passed through the fixed layer, a spin current is generated that tunnels into the free layer producing torques on the magnetization. These torques are known as anti-damping torques and along with the equilibrium torques (caused primarily by the Oersted field produced by the charge current) will cause the magnetization to precess [9]. The anti-damping torque will cause greater and greater precession which will result in flipping with a sufficiently large torque [5].

The magnetization direction can be measured utilizing tunneling magneto resistance (TMR). Because magnets are spin polarized, there are more states available for specific spins. If spin current is passed through with direction that is parallel (P) to the magnetization, then there will be relatively low resistance because there are many states available. If spin current with direction anti-parallel (AP) to the magnetization is passed through, there will be relatively large resistance [5, 6]. Performing this measurement requires little current and values of the TMR ratio (Eq 1) of over 1000% have been measured [4].

$$\text{TMR Ratio} = \frac{R_{AP} - R_P}{R_P} \tag{1}$$

The TMR Ratio defines the change in resistance for spin polarized current flowing into a magnetic layer for AP and P orientations.

Research on STT-MRAM devices has primarily focused on free and fixed layers with in-plane magnetization [3–5]. However, in-plane magnets have low thermal stability. Thermal energy can cause the magnetization of a material to flip which is a problem if STT-MRAM is to be non-volatile. The energy needed to flip from one magnetization to another is defined by the energy barrier (E_b) between the two desired orientations. The commercial requirement for long-term storage requires a ten year
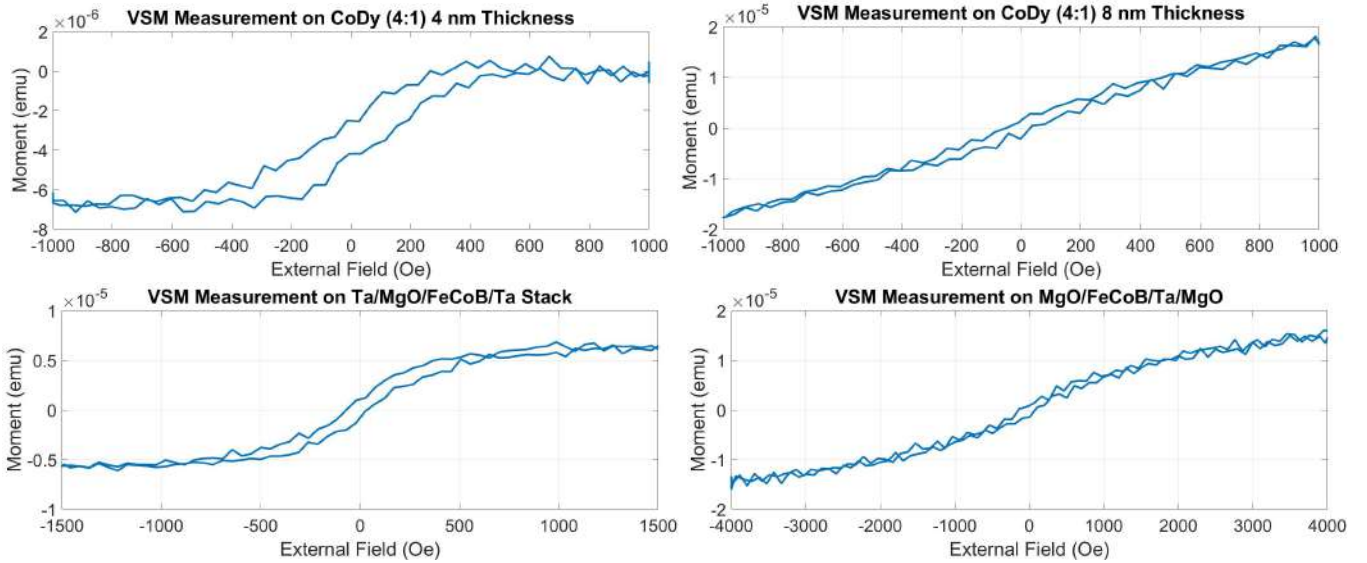
FIG. 3. VSM measurements on potential PMA samples. The 4 nm CoDy and Ta/MgO/FeCoB/Ta stack display signs of PMA not found in the 8 nm CoDy or MgO/FeCoB/Ta/MgO samples.

interval to pass before it is possible for magnetization to flip due to thermal energy; MTJ stacks with in-plane magnets do not meet this requirement [3, 4]. This is because it is relatively easy for the magnetization to rotate in the plane of the free layer. The smaller a bit can be made, the more information can be stored. When STT-MRAM utilizing in-plane ferromagnets are scaled below 50 nm, the thermal instability becomes a problem. Using elliptical shapes for the device can increase the thermal stability but this fix is insufficient below 22 nm [3].

Using a magnet with perpendicular magnetic anisotropy (PMA), out-of-plane magnetization, for the free layer will provide the desired thermal stability for scaling below 50 nm. However, the anti-damping torques used for switching the in-plane free layer were in-plane. For an out-of-plane free layer, an out-of-plane anti-damping torque would be needed to flip the magnetization. This will require a different fixed layer to generate spin currents that will apply the needed torques. Novel materials such as MgN could be explored to determine whether they generate out-of-plane anti-dampening torques. A fixed layer with PMA that is exchanged biased with an antiferromagnetic layer may also provided the needed torques.

III. FERROMAGNETIC THIN FILMS WITH PERPENDICULAR MAGNETIC ANISOTROPY

A fixed layer with PMA cannot be used by itself to induce torques on the free layer. This is because the net spin, used to switch the free layer, points out of the material's plane. SHE will then create a spin current that flows perpendicular to the current and spin direction which will be in the plane of the fixed layer so these

spins will not reach the free layer. In order to utilize a fixed layer with PMA, its magnetization must have some in-plane component allowing the spin current to flow diagonally upward. This can be done with an external field.

It was found by Ref [10], that an antiferromagnetic material could be used for exchange biasing the fixed layer of an MTJ and allow for tuning of the spin current flowing into the free layer. By placing the antiferromagnetic material below the fixed layer in the stack then heating past the Néel temperature with an external field applied, the top layer of the antiferromagnet will align with the external field and will remain in this state after returning to room temperature. This magnetization is weak and has only a noticeable effect a few nanometers above the surface enough for tilting the magnetization of the fixed layer downwards but having no observable effect on the free layer.

This investigation attempted to grow ferromagnetic materials with PMA using a mixture of Dysprosium (Dy) and Cobalt (Co) and a stack of Iron Cobalt Boron ($Fe_{60}Co_{20}B_{20}$) and Magnesium Oxide (MgO). CoDy layers with ratios of 1:4, 1:3, and 30:70, respectively, were grown with material thicknesses of 4 nm and 5 nm. Additionally, a film of thickness 8 nm was grown with a ratio of 1:4. All CoDy samples were grown over and capped with 1.5 nm of Tantalum (Ta). The following stacks of FeCoB and MgO were grown: Ta(5)/FeCoB(1)/MgO(1.8)/Ta(1) and MgO(1.5)/FeCoB(1)/Ta(1.5)/MgO(3). Number in parenthesis dictates thickness in nanometers. All films were grown using DC magnetron sputtering. After growth the MgO, FeCoB, and Ta stacks were annealed at 260 °C for one hour. All PMA measurements were performed using vibrating sample magnetometer (VSM) measurements. This measurement is done by applying
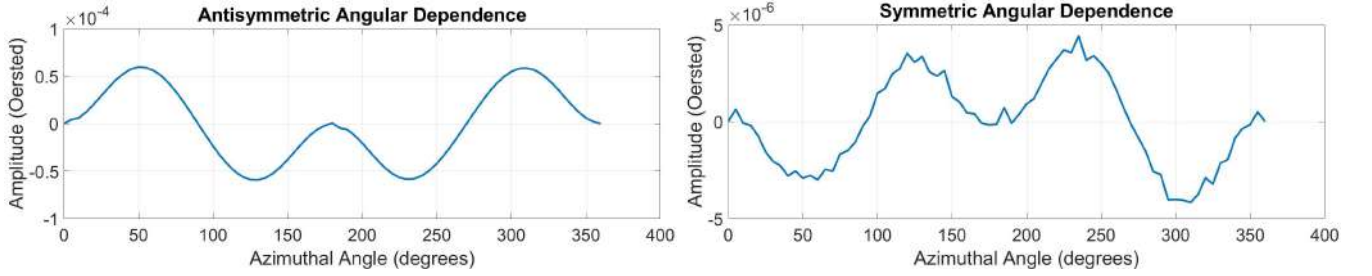
FIG. 4. ST-FMR measurements on MgN sample grown on silicon crystal lattice. Shape of symmetric and antisymmetric components follow $A*Sin(\theta)^2*Cos(\theta)$.

an external magnetic field perpendicular to the sample's plane and measuring the magnetic moment. Samples with observable hysteresis curves will have PMA.

The results from the VSM measurements are shown in Fig 4. The 4 nm thick CoDy sample displayed signs of PMA while the 8 nm thick sample did not. However, the width of the hysteresis curve for the 4 nm thick sample is small. After literature review, it was found that the films grown may have been too thick. Other researchers were able to create PMA films with DyCo stacks on the scales of a nanometer or less. It is reported that interface effects give rise to PMA and thicker films can cover up this effect [11]. The sample grown in this investigation has a much smaller hysteresis curve compared to the samples grown in Ref [11]. Films of similar thickness to those reported if Ref [11] will be grown in the future.

The Ta/MgO/FeCoB/Ta stack did display signs of PMA while the MgO/FeCoB/Ta/MgO either does not display signs of PMA or displays signs of weak PMA. Now that materials with PMA have successfully been grown, the next step to be undertaken will be to make the MTJ devices outlined earlier.

IV. SAMPLES WITH MAGNESIUM NITROGEN

MgN is of interest because of its peculiar magnetic ordering. It was obtained from Chang-Beom Eoms group at the University of Wisconsin-Madison researching spin torque in novel material structures. The Ralph group was asked to perform characterization of the samples produced in hope that this material may be able to generate nonstandard torques when current is passed through. A layer of Py serves as the sensor layer for measurements.

Spin-Torque Ferromagnetic Resonance (ST-FMR) measurements, a standard technique used to discern the torques and spin hall angle (ratio between spin current and charge current), was used to characterize the torques being produced from the spin current generated from MgO. This measurement technique works by applying an RF current to the sample and scanning and external magnetic field. Measuring the mixing voltage will produce the signal seen in Fig 5. This signal is composed of a symmetric and antisymmetric lorentzian. If the field is

scanned multiple times with the external field at different angles with respect to the sample, an angular dependence for the symmetric and antisymmetric components can be found. The shape of the angular dependence of the components determines what torques were present.
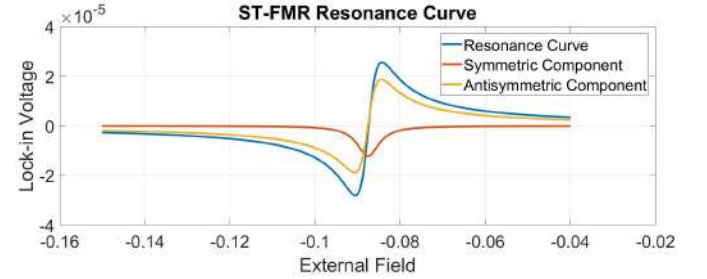

FIG. 5. Example ST-FMR signal in blue. This signal is composed of a symmetric lorentzian (yellow) and an antisymmetric lorentzian (red) component. The angular dependence of these components, with respect to external field and the sample, will determine the torques present.

Fig 3 shows the ST-FMR data for our MgN samples. The torques generated from the spin current are found in the symmetric component which has the shape of $A*Sin(\theta)^2*Cos(\theta)$. Given this shape, there are no nonstandard torques being generated from MgN. Further ST-FMR measurements with MgN will be taken at different temperatures because MgN will have transitions in magnetic ordering at different temperatures.

V. CONCLUSION

Films with PMA were succesfully grown. In the future, samples similar to Ref [11] will be made to determine if stronger PMA can be obtained. Once strong PMA values have been found, MTJ devices utililzing CoDy for the fixed layer and the Ta/MgO/FeCoB/Ta stack for the free layer will be fabricated. The CoDy films will be used for the free layer because it has lower restivity so more charge current will flow through it allowing more spin current to be generated.

Additionally further characterization of MgN will continue. Because MgN has transitions in magnetic order-

ing at different temperatures, ST-FMR measurements for different temperatures will be performed to see if any of these other orderings produce nonstandard torques.

VI. ACKNOWLEDGMENTS

[1] Alex Ryckman Mellnik. *Measurements of Spin Torques generated by Topological Insulators and Heavy Metals.* A Dissertation of Cornell University, (2015).

[2] *STT-MRAM Products.* Everspin Technologies.

[3] L. Thomas, G. Jan, J. Zhu, H. Liu, Y. J. Lee, S. Le, R. Y. Tong, K. Pi, Y. J. Wang, D. Shen, R. He, J. Haq, J. Teng, V. Lam, K. Huang, T. Zhong, T. Torng, and P. K. Wang. *Perpendicular Spin Transfer Torque Magnetic Random Access Memories with High Spin Torque Efficiency and Thermal Stability for Embedded Applications.* Journal of Applied Physics **115**, 172615 (2014).

[4] S. Bhatti, R. Sbiaa, A. Hirohata, H. Ohno, S. Fukami, S. N. Piramanayagam. *Spintronics based random access memory: a review.* Materials Today, 20 (2017).

[5] D. C. Ralph and M. D. Stiles. *Current Perspectives: Spin Transfer Torques.* Journal of Magnetism and Magnetic Materials, 320 (2008).

[6] J. Gibbons. *Measurements of Spin Torques due to Reorientable Anomalous Hall Spin Current* A Dissertation of Cornell University, (2018).

[7] A. Hoffmann. *Spin Hall Effects in Metals.* IEEE Transactions on Magnetics **10**, 49 (2013).

[8] F. Hellman, A. Hoffmann, Y. Tserkovnyak, G. Beach, E. E. Fullerton, C. Leighton, A. H. MacDonald, D. C. Ralph, D. A. Arena, H. A. Dürr, P. Fischer, J. Grollier, J. P. Heremans, T. Jungwirth, A. V. Kimel, B. Koopmans, I. N. Krivorotov, S. J. May, A. K. Petford-Long, J M. Rondinelli, N. Samarth, I. K. Schuller, A. N. Slavin, M. D. Stiles, O. Tchernyshyov, A. Thiaville, B. L. Zink. *Interface-induced phenomena in magnetism.* Reviews of Mdern Physics, 89 (2017).

[9] N. R. Reynolds *Controlling Spin Orbit Torques through Strong Correlation.* A Dissertation of Cornell University, (2018).

[10] J D. Gibbons, D. MacNeill, R. A. Buhrman, and D. C. Ralph. *Reoreintable Spin Direction for Spin Current Produced by Anomalous Hall Effect.* Physical Review Applied **9**, 064033 (2018).

[11] Z. S. Shan and D. J. Sellmyer. *Magnetism of Rare-EarthTransition-Metal Nanoscale Multilayers. I. Experiments on Dy/Co, Dy/Fe, and Tb/Fe.* Physical Review B **16**, 42 (1990).

[12] A. E. Freitag and A. R. Chowdhury *Effect of Interface on Magnetic Anisotropy of Fe/Tb Multilayers: Mössbauer Effect Study.* Journal of Applied Physics **82**, 5039 (1997).

Magnetic Handshake Materials

Richard Liebert[1,2], Edward Esposito[2,3], Ran Niu[2,3], Sloane Amato[2], and Itai Cohen[2,3]

[1]Northeastern University, Boston, Massachusetts
[2]Cornell Center for Materials Research, Cornell University, Ithaca, New York
[3]Laboratory of Atomic and Solid State Physics, Cornell University, Ithaca, New York

Self-assembly is a useful technique for constructing complex objects at the nano- and microscale. We aim to develop magnetic materials capable of self-assembling, with the ultimate goal of creating microscale building blocks that allow easy programming and manipulation of the self-assembly process. Using magnets as the driving components in our system is ideal due to the long-range nature of magnetic forces, as well as the relative ease with which they can be designed and their ability to function well on both the macroscale and microscale. While past work on microscale magnetic self-assembly has focused on components featuring simple dipole-dipole interactions, we intend to explore the interactions of complex magnetic patterns ("handshakes") at the microscale.

I. INTRODUCTION

Self-assembly is the process by which particles will spontaneously arrange themselves into ordered structures with little external direction. Self-assembly is widely employed in nature, especially in biological processes such as protein synthesis. With the ever-growing push for smaller and smaller technologies straining current small-scale manufacturing techniques, self-assembly processes have received interest and study as a possible nanoscale manufacturing technique with broad potential applications. Due to their ability to function well at both the macroscale and nanoscale, magnetic forces are especially promising as potential drivers of self-assembly. In this paper, we study a macroscale system that is analagous to systems we hope to study at the microscale. Physical vibrations caused by a shaker in this work are analogous to thermally exciting a system at the nano- or microscale. Past work, such as that by Stambaugh et al. [1,2] has shown that by mechanically "thermalizing" systems of magnetic particles, reversible self-assembly into ordered structures can be observed as well as self-segregation behaviors between particles featuring attractive forces of different magnitudes. However, this and other past work (such as that by Ilievski and Whitesides et al. [3], Pál et al. [4], and Hageman et al. [5]) has focused only upon simple dipole-dipole magnetic interactions. We seek to explore particle systems featuring complex magnetic patterns which allow for many types of interactions. We hope that this allows us to not only recreate those reversible self-assembly and self-segregation behaviors previously shown but to allow for myriad complex ways to program, manipulate, and control the self-assembly process itself. Ultimately, we intend for this macroscale study to lay the groundwork for more novel research to be done at the nano- and microscale using nanofabrication and lithography techniques at the Cornell NanoScale Science and Technology Facility (CNF).

II. MATERIALS AND METHODS

A. Particles

Our objective was to design self-assembling building blocks with complex patterns of magnets that allow for different types of interactions. We used cylindrical, rare earth (Neodymium) magnets 1/16" in diameter and 1/8" in height, dropped into four holes forming a square in a laser-cut cylinders of acrylic 9mm in diameter and 1/8" tall. Since these "particles" each featured a 4x4 array of magnets, there are four unique patterns possible (everything else can flip or rotate to one of these) which we have arbitrarily color-coded white, green, blue, and red as shown in Fig. 1.
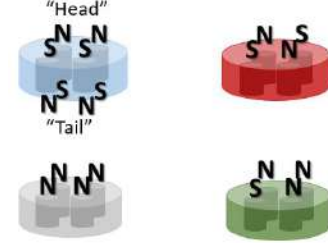

FIG. 1. The four types of particles, color coded.

Particles are attracted to those of the same type most strongly in a "head-to-tail" orientation in which the circular surfaces of two cylinders line up face to face with one another, however same-type bonds vary in strength for each particle type. For example, the strongest bond is that between two white particles, the next strongest is between two green, followed by blue, and the weakest bonds are between red particles. Magnets are held in place in their acrylic disks using super glue, and each complete disk was spray painted according to our color coding scheme. With the particles in this configuration, the formation of the weaker "incorrect" bonds, in which two pieces of different types bond together or pieces of the same type bond in a non head-to-tail orientation was

possible due to the raw strength of the interactions between the magnets when their bare surfaces are exposed. To decrease the strength of the magnetic interactions so that incorrect bonding configurations could reliably be broken in our apparatus, we glued a single 1/16" tall cylinder of acrylic with the same diameter as our disks onto the top and bottom of each disk, covering the exposed area of the magnets. After extensive prototyping, it was determined that these 1/16" "spacers" were the optimal size to allow the correct same type head-to-tail bonding to initiate a self-assembly process without enabling incorrect bonds that were too strong to be easily broken in our apparatus.

B. Apparatus

After fabricating our self-assembling pieces, we began our experimentation by putting a homogeneous mixture of the blue pieces into a transparent, acrylic box 4" in height and 6" by 6" in length and width. This box was then screwed on top of a Brüel & Kjaer Vibration Exciter type 4809 (shaker) (soon to be replaced with the more powerful type 4808), with a Teflon cylinder acting as a spacer between the box and the shaker. This shaker vibrated with varying amplitude and frequency. We fed the shaker energy via a Brüel & Kjaer Power Amplifier type 2718 (soon to be replaced by the more powerful type 2719) where wattage and thus vibration amplitude could be controlled. The amplifier in turn received input from a BK Precision 3011B Sine Function Generator on which we could control signal frequency. The shaker was clamped down onto a table to prevent movement. A Logitech webcam placed on a tripod pointing down towards the apparatus was used to capture video and images at specific intervals for some experiments. This complete apparatus is shown in Fig. 2.
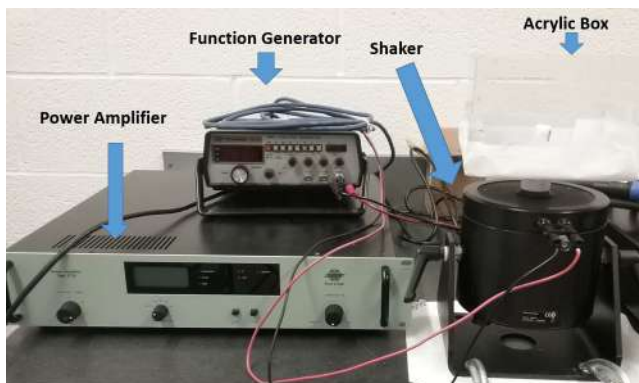

FIG. 2. Our apparatus.

C. Experimentation

Upon providing power to the shaker and changing the amplitude and frequency of the vibrations, the particles were observed to bond together as predicted, self-assembling into long chains consisting of many blue particles bonded head to tail into a single long cylinder, analogous to a polymer. At some especially low amplitudes, these self-assembled chains would interact with one another by sticking together side by side, since there exists a mild attractive force between particles horizontally in certain orientations. The size of these chains of particles varied but at low amplitude settings they would reach as large as about 20 particles, a large enough chain to stretch across an entire dimension of the box side to side, while they were sometimes as small as two particle "dimers", and most chain sizes fell somewhere in between. A comprehensive study of the distribution of chain sizes has not yet been conducted. As amplitude rose and the particles bounced up and down, these chains eventually began to break up as particles at either end of a chain saw their bonds broken due to collisions of increasing intensity with the bottom surface and walls of the box. In addition, chains of pieces would sometimes split at some point midway across due to a collision, which resulted in either two smaller chains then moving independently or in the shattering of the entire length of the chain into independent particles with no bonds, "monomers". Upon further exploration of this change in behavior, we learned that at low amplitudes virtually all of the particles would ultimately end up in a chain bonded with at least one neighbor while at high amplitudes virtually every particle would become and remain independent and bonds would not be sustainable. We determined that it would be beneficial to study this change in behavior as analogous to a phase transition; hereafter, states where the dominant behavior of particles is forming and maintaining bonds will be referred to as "solid", while states where the dominant behavior is to break bonds and fly around independently will be referred to as "gaseous". Examples of snapshots taken of a system of red particles in the gaseous and solid states are shown in Fig. 3. The transition to a gaseous state was observed
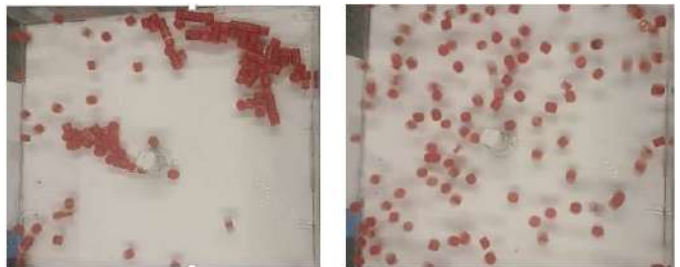

FIG. 3. Snapshots of a system of red particles in the solid phase (left) and the gaseous phase (right).

to happen most easily at frequencies between about 20

and 40 Hz. At frequencies lower than this, our particles would stay flush with the bottom of the box regardless of amplitude, while at frequencies above this range the particles would not experience powerful enough collisions to break bonds. This is likely because they did not have time to respond to the extremely fast oscillations and did not bounce very high as a result. For the purposes of these experiments we decided to set frequency at 30 Hz moving forward, since we were interested in investigating changes in this self-assembly behavior in relation to the acceleration experienced by the particles and considered frequency to be a minor detail of our setup.

III. RESULTS AND DISCUSSION

Once we had determined through qualitative observation that a phase transition exists, the next logical step was to quantitatively define those phases. To do this, we ran experiments in which a system of particles began at a high amplitude, gaseous phase and then were "cooled" to a lower amplitude solid phase very quickly, while recording snapshots at 8 Hz using the webcam. The webcam pictures were analyzed by manually counting the number of particles that experienced any bonding with neighbors (were part of chains) or did not at all (were monomers) in specific frames. We plotted the fraction of pieces that were monomers labeled as the gaseous fraction and the remaining portion of pieces as the solid fraction as a function of time. When the final amplitude setting is low enough, the system will reach an equilibrium with greater than 90% of the particles in the solid state, with most of the transition activity occurring in the first five seconds, as shown in Fig. 4. On the other
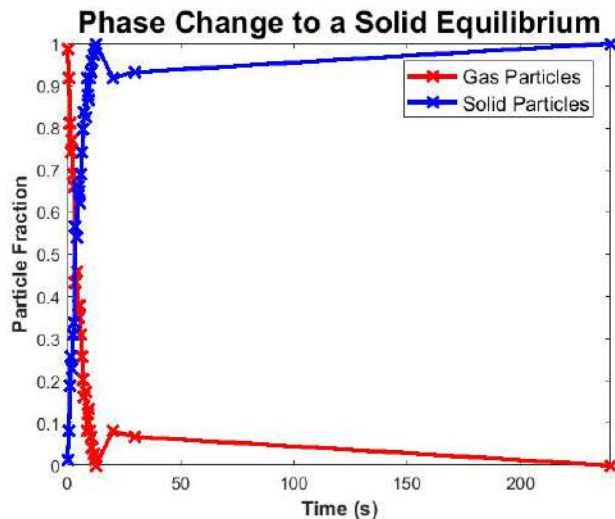

FIG. 4. Reaching an equilibrium in the solid state.

hand, when the system is cooled to an amplitude that is very close to the gaseous region, it will reach an equilibrium where there are significant numbers of particles in

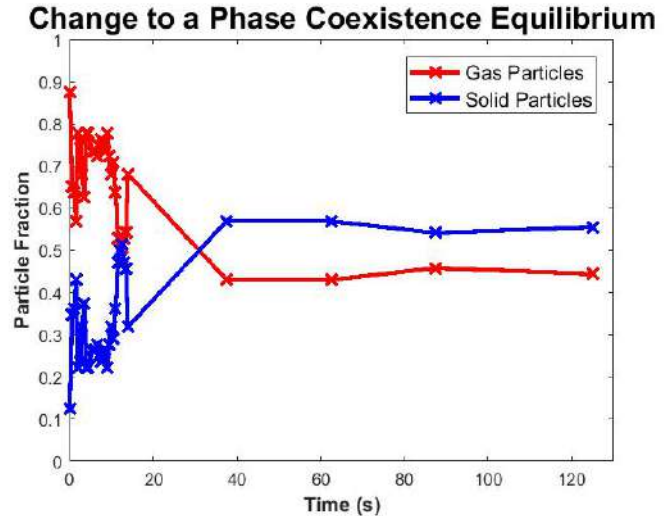both the gaseous and solid state, as shown in Fig. 5. This

FIG. 5. Reaching an equilibrium where solid and gaseous phases coexist.

demonstrates that the threshold between the two states is not clear-cut, and there exists some phase transition region in which gaseous and solid behavior coexisted in equilibrium. Based on our data, we determined that the system was definitely in the solid phase if at least 90% of the particles had at least one bond and was gaseous if at least 90% had no bonds, while describing everything in between as a transition state. The significant size of the coexistence region presents a number of interesting possibilities for better controlling self-assembly processes by allowing us to cause such a reaction to only partially complete. Subsequently, we changed various parameters in an attempt to manipulate this phase transition, starting by increasing the number of particles in the box thus increasing the area fraction of our system. By doing this, it appeared that a higher amplitude was required in order to initiate the phase transition. Seeking to better understand this relationship, we ran various tests and constructed a "phase diagram" of the system of blue particles in Fig. 6. The lower line in this graph represents the beginning of the coexistence region and the upper line represents the end of it. Above the coexistence region is the gaseous phase, and below it lies the solid phase. The y-axis is in units of gs (9.81 m/s^2) of maximum acceleration experienced by the box, which is proportional to amplitude, while the x-axis is in units of particles in the box (essentially area fraction of the system). Values of g are logical to compare since accelerations below a single g should theoretically be counteracted by gravity and fail to result in any motion of the particles. Currently, values of g are approximate relying on a relationship between wattage provided to the speaker and resultant amplitude that was studied manually using a ruler. In the future, we hope to use an accelerometer that we do not yet possess to accurately measure maximum acceleration
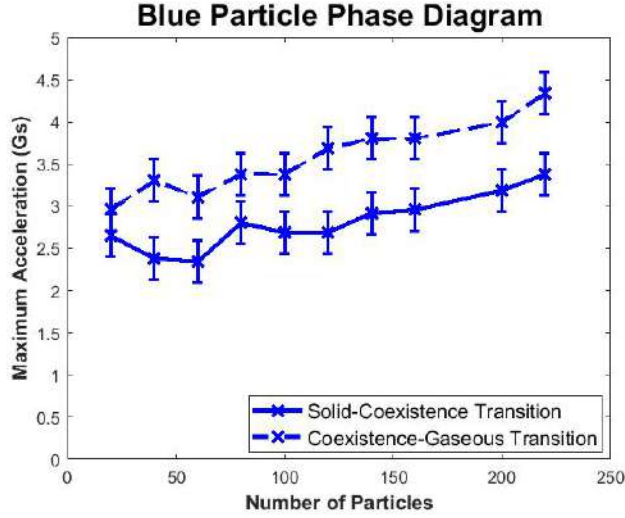
Blue Particle Phase Diagram

FIG. 6. "Phase Diagram" of blue particles.

in each experiment. The approximately linear relationship shown should be investigated further in the future at higher orders of magnitude with respect to number of particles (area fraction), since this relationship could have powerful implications when fabricating thousands or millions of these on the nano- and microscale. Since up until now we have only used the blue particles, we next tried these same experiments with the red particles (green and white particles could not be broken up by our current apparatus), resulting in the graph shown in Fig. 7 (points represent the approximate middle point of the phase coexistence region, calculated using the mean of the bottom and top of points of said region).

This graph shows that each type of particle has a unique phase transition line related to the strength of the bonds it forms. Up to this point, our experiments had
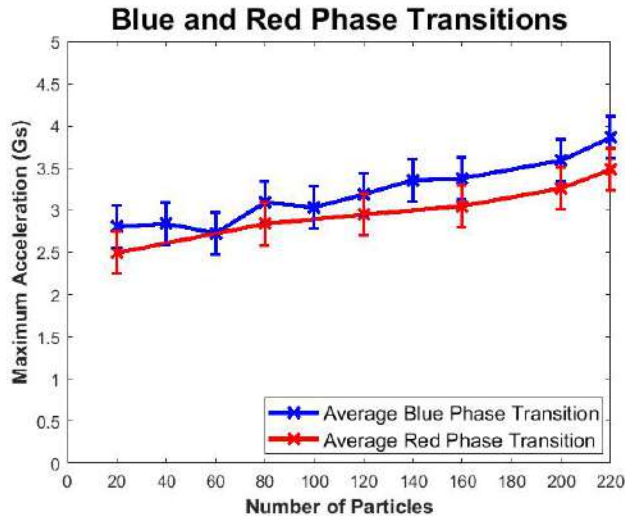
Blue and Red Phase Transitions

FIG. 7. Phase Diagram of blue and red pieces).

exclusively investigated homogeneous mixtures where all of the particles were of the same type. Our naïve expectation was that particles of different types will interact with each other minimally when put together and display independent phase transitions. To test this, we mixed red and blue particles at a fixed particle number and mapped the phase transition of each particle type with different ratios of each in the mixture, as shown in Fig. 8. Once again, the data points represent the
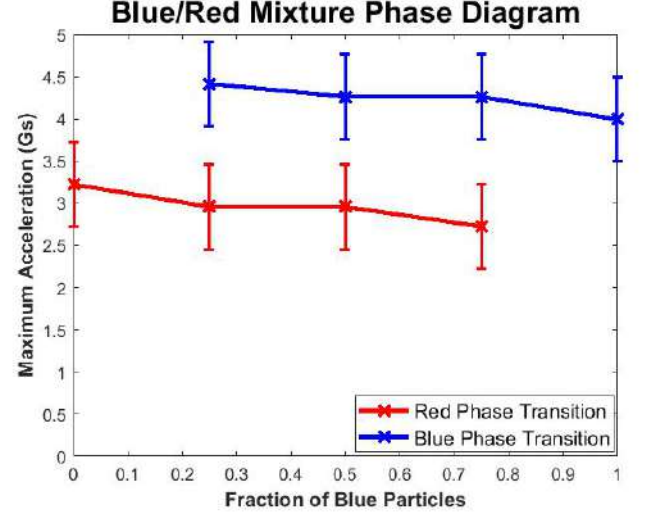
Blue/Red Mixture Phase Diagram

FIG. 8. Phase Diagram of a heterogeneous red/blue mixture with variable composition and constant area fraction.

approximate midpoint of the coexistence region. Our results here suggest that the phase transition of particles in heterogeneous mixtures is virtually the same as it is when particle types are alone, suggesting that they do not interact with particles of a different type much and that whatever interactions exist across types are insufficiently strong to affect same type interactions. In addition, our naïve expectation regarding independent phase transitions was actually proven correct, as at settings between the two phase transition curves all the blue particles would settle into a solid state while red particles remained gaseous. This constitutes both a self-segregation behavior and an avenue through which we may be able to control the order of a self-assembly process. Another way in which we tried to manipulate the phase transition was by applying a magnetic field to the box. Since our particles are magnetic, it intuitively makes sense to investigate the effects of magnetically perturbing them. Upon waving a magnet outside the box with my hand while the speaker was active, we observed that particles in the region being affected by the magnetic field were able to form bonds even at amplitude settings that would typically induce the gaseous phase. We believe that this is because particles will all be arranged in the same orientation by the magnetic field, which means that bonds are more likely to form since particles are biased towards an orientation in which collisions are more likely to result in

new bonds. We have not yet been able to take thorough data on how this changes the phase transition since we have not yet constructed an apparatus capable of applying a uniform magnetic field to the entire box. Another layer of complexity can be added to the system with the introduction of "Janus particles", which have different magnetic patterns on each side (Fig. 9), resulting in different strength bonds being formed on each side of the particle. This results in a number of interesting prop-
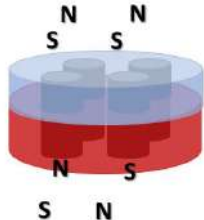

FIG. 9. A red/blue "Janus particle".

erties that can be observed qualitatively. For instance, since they have a different bond strength on each side, the phase transition happens at a different point for each side. This means that at some higher amplitude setting Janus particles might begin sticking together in twos as the stronger bonding site becomes active, while at a much lower amplitude those dimers begin to actually bond together and create longer chains as the weaker bonding site becomes active. Thorough data on this has not been taken either yet, due mostly to how time consuming and difficult the creation of Janus particles is. It is worth noting that when constructing a Janus particle, the specific orientation of each magnet is more relevant than when creating standard particles since one pole of each magnet is embedded within the disk, where the interactions it can experience with external particles are minimal. In addition, while the Janus particles in Fig. 9 show the two magnetic patterns directly on top of each other, it is possible to rotate either one of these patterns any number of degrees relative to the other before applying glue, introducing even more possible configurations for these particles. This effectively means that for each combination of two particle types, there exist many possible distinct Janus particle configurations each with slightly different bonding strengths and properties. Determining which orientations are ideal to mass produce for our work remains an ongoing process.

IV. FUTURE DIRECTIONS

This project is still in early exploratory stages, and as such there is a wealth of work that should be done in the future. Firstly, exploring pieces with new geometries and different arrays of magnets should be investigated in a few different ways. By introducing larger arrays of magnets, it is possible that we can create more and more distinct bond strengths, which in turn could lead to an entire spectrum of phase transitions that allow precise control of the order of bonding in a self-assembly process. In addition, introducing magnets both in and out of the plane perpendicular to each other could allow for more complex three dimensional shapes, or potentially for the encoding of information in one plane while bonds in another plane form a backbone analogous to a DNA structure. Prototyping of particles like these is already underway and early results seem promising. Secondly, expanding upon our work with Janus particles to see if we can actually create a "controlled polymerization" reaction whereby chain size can be controlled accurately by changing the applied power may be an important direction for further work. Exploratory work in this area has led us to believe that with many more Janus particles this may be possible, and it could represent yet another promising way to influence the self-assembly process. Thirdly, we do intend to eventually bring all of this work into the nanoscale at the CNF with the help of collaborators in the McEuen group, which is where we hope true breakthroughs in nanotechnology will emerge.

V. CONCLUSION

We have shown that magnetic self-assembly systems featuring complex arrays of magnets at bonding sites successfully presents many new ways to manipulate and control the self-assembly process at the macroscale. In the future, we hope to further explore the unique behaviors and possibilities these systems enable and to replicate this work on the micro- and nanoscale.

VI. ACKNOWLEDGEMENTS

[1] J. Stambaugh, Z. Smith, E. Ott, and W. Losert, Phys. Rev. E 70, 031304 (2004).

[2] J. Stambaugh, K. V. Workum, J. F. Douglas, and W. Losert, Phys. Rev. E 72, 031301 (2005).

[3] F. Ilievski, M. Mani, G. M. Whitesides, and M. P. Brenner, Phys. Rev. E 83, 017301 (2011).

[4] G. Pál, F. Kun, I. Varga, D. Sohler, and G. Sun, Phys. Rev. E 83, 061504 (2011).

[5] T. A. G. Hageman, P. A. Löthman, M. Dirnberger, M. C. Elwenspoek, A. Manz, and L. Abelmann, J. Appl. Phys. 123, 024901 (2018).

Covalent Immobilization of Proteins on Electrospun Nanofibers for Biosensor and Biomedical Applications

Matthew Molinaro[1], Mesbah Najafi[2], Michael Delaney[3], Margaret W. Frey[2]

1   Department of Biomedical Engineering, University of Florida, Gainesville, FL 32611, USA
2   Department of Fiber Science and Apparel Design, Cornell University, Ithaca, NY 14853, USA
3   Chemical and Biomolecular Engineering Department, Cornell University, Ithaca, NY 14853, USA

Abstract: In this work, plasma treatment was used to functionalize the surface of electrospun poly(lactic acid) (PLA) nanofibers for protein immobilization. To achieve this, the effect of various plasma treatment parameters such as voltage and time on the chemical structures of the nanofibers fabrics was studied. Methylene blue adsorption analysis was used to characterize the surface chemistry of the nanofibers. Protein binding to the nanofibers surface was examined by static and dynamic adsorption tests. BSA was used as a model protein for this study. The adsorption tests were also conducted on poly(vinyl alcohol)/poly(methyl vinyl ether-alt-maleic anhydride) (PVA/PMA) nanofibers for comparison. Oxygen plasma treatment effectively created carboxylic acid functional groups on the surface of the PLA fibers. The data also showed that a dynamic binding of protein to PLA via bioconjugation chemistry yielded the best results in terms of maximizing specific covalent binding and minimizing non specific adsorption. Static binding of protein led to high levels of nonspecific binding for both PLA nanofibers and PVA/PMA. Covalent binding of proteins on nanofibers can allow for high sensitivity biosensing thanks to high surface area and porosity of nanofiber fabrics. The results obtained widen the biomedical applications of PLA.

Keywords: nanofibers, poly(lactic acid) PLA, oxygen plasma treatment, proteins, biosensor , electrospinning

---

1. Introduction

Biosensor devices are critical to successful biochemical research and diagnostics [1]. Biomarkers (proteins, peptides, hormones, etc.) levels can change in relation to disease state and pharmaceutical intervention. Highly sensitive quantification is an essential part of research and accurate diagnoses [2]. Enzyme linked immunosorbent assay (ELISA) is a common method for quantifying biomolecules [2,3]. ELISA typically involves physical adsorbing an antigen or antibody to a flat plastic surface then the successive administration of antibodies, target biomolecules, and signal producing species. For example, a sandwich ELISA involves the immobilization of an antibody on a flat surface followed by the administration of antigen containing solution. This solution is then washed away and another antigen binding antibody known as the secondary antibody is administered. An antibody linked to a signal producing species (i.e. enzyme) is then bound to the secondary antibody. Finally, the substrate for the enzyme is added and the absorbance of the resulting solution can be taken and compared to standards to quantitatively estimate the concentration of a particular biomolecule [2]. One of the main issues with this ELISA method is the physical adsorption of an antigen or antibody to a flat surface. This can lead to loss of function, leeching of biomolecule from the surface, and inconsistent distribution [2,3]. One possible solution to this problem is through the use of nanofibers (NFs). NFs have large surface area, porous structure, and good mechanical properties [1-4]. Additionally, polymer NFs can under go a variety of

surface modifications including and not limited to plasma treatment, chemical modification, and polymer grafting [1-3, 5-9]. These properties make NFs good candidates for biomolecule immobilization.

Electrospinning of NFs has gained increasing popularity over the decades for its ease of processing and quality of fibers produced [5]. Electrospinning involves using a high voltage source connected to a syringe extruding a conductive polymer solution and a grounded collector plate. The high voltage draws out fibers between the syringe tip and the collector plate. Typically, NFs collect as a woven mat. The properties of the collected NF mat can be altered by changing the extrusion speed of the solution, voltage of the power source, distance between the syringe needle and the collector, and the concentration of polymer in the solution [10]. Figure 1 illustrates the basic set up for an electrospinning operation.
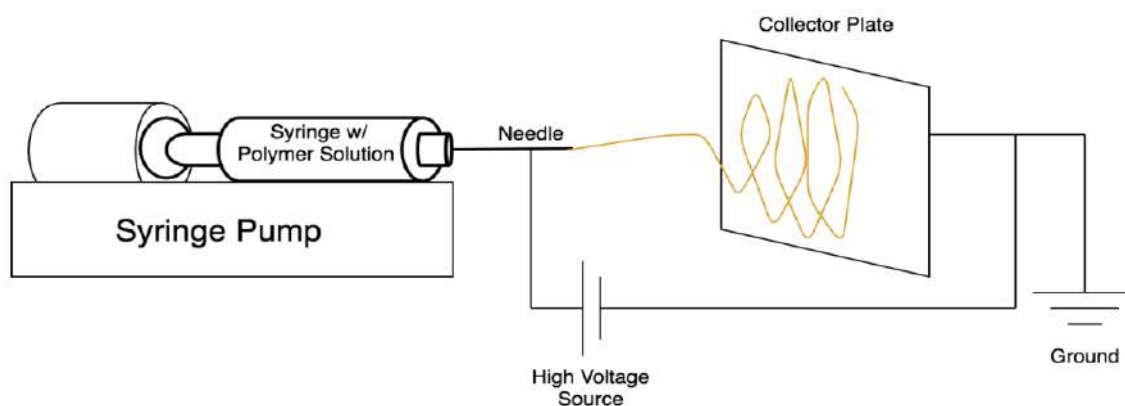


Figure 1. Scheme of electrospinning process

Electrospun NFs have been used in a variety of purposes including advanced ELISA, protein capture, microbe capture, and tissue engineering [2,4, 6-9,11]. Hosseinzadeh et al. [2] covalently attached antibodies to polyethersulfone NF meshes and was able to gain higher intensity ELISA signals when compared to traditional methods. The higher intensity signals lead to higher sensitivity assays. Najafi et al. [4] utilized charged electrospun NF meshes for the selective binding of proteins based on electrostatic properties. Matlock-Colangelo [11] covalently bound antibodies to NFs for the capture of E. coli cells. Schofer et al. [9] bound RGD peptides to biocompatible NFs for the growth and differentiation of stem cells.

PLA is a biodegradable and biocompatible natural polyester [14]. PLA can be fashioned into NFs via electrospinning [1,3,6-10,14,15]. PLA contains no free carboxyl groups in its intrinsic form. In order to introduce carboxyl groups on PLA NFs, oxygen plasma treatment can be performed to modify the surface of the NFs [6,7,9]. Previously hydrophobic PLA NFs become more hydrophilic after plasma treatment [6,7,9,15]. This chemical change is indicative of the addition of carboxyl groups. The PLA NFs activated by the plasma can now participate in the formation of the semi-stable amine reactive sulfo-NHS ester. PLA modified with surface protein can have application ranging from biosensing to tissue engineering [6,7,9,15]. Biosensing could simply be the isolation of amine presenting species as well as utilizing of interactions such as the well studied biotin-avidin interaction [15]. The avidin protein can be bound to the NF and then the NFs could be used to filter out or isolate biotinylated species. PLA's biocompatibility and biodegradability have made its NFs applicable for bone tissue engineering, stem cell engineering, and cartilage tissue engineering [6,7,9,16].

Another promising multi-functional polymer NF system is the PVA/PMA blend. Similar to PLA,

PVA/PMA blends can be electrospun into NF fabrics [4,11]. The PVA portion of this blend makes the fibers extremely hydrophilic [4]. The highly hydrophilic nature will allow water based solutions to easily travel through the porous NF structure giving dissolved molecules in the solution better opportunity to bind to the fibers or functional groups on the fibers [4,11,15]. Additionally, the PMA portion of the fibers contains anhydride groups that can be hydrolyzed to form carboxyl groups [4]. These carboxyl groups can be reacted with sulfo-NHS/EDC chemistry to allow the fibers to bind proteins covalently. PVA/PMA has been used to electrostatically sort proteins and covalently bind microbe antibodies for selective capture [4,11]. Ideally the PVA/PMA fibers, with their intrinsic hydrophilic nature, will be good candidates for enhanced biosensing applications as well as protein filtration and purification.

In this study, we examined the use of bioconjugation chemistry on NFs for the binding of proteins. Specifically, 2 polymer NF systems were investigated. The first being PLA and the second being a PVA/PMA blend. PVA/PMA presents carboxyl groups without plasma treatment and will be used to compare results of plasma treated PLA. Both polymer systems were modified with sulfo-NHS/EDC bioconjugation chemistry. Sulfo-NHS/EDC bioconjugation allows for the cross linking of amide presenting species with carboxyl presenting species [12]. Sulfo-NHS/EDC chemistry has been applied to the crosslinking of proteins to NFs, functionalization of nanoparticles, and creation of immunoassays [2, 9,13,12]. The bioconjugation works by binding EDC to a carboxyl group forming a reactive o-acylisourea ester. Sulfo-NHS can then be reacted with the ester to form a semi-stable amine reactive sulfo-NHS ester which can then react with amine groups, commonly present on proteins [12]. Figure 2, inspired by Vashist, diagrams the chemical reactions that take place during sulfo-NHS/EDC conjugation on NFs.
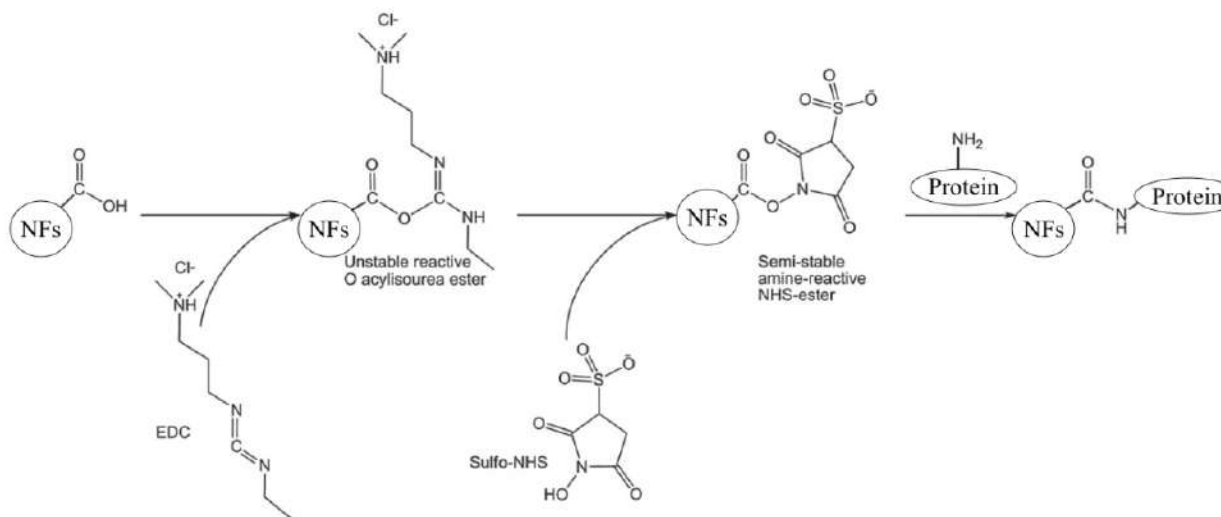
Figure 2. Sulfo-NHS and EDC conjugation reaction

2. Materials and Methods

2.1. Materials:
PLA 4043D (MW: 150 KD) was purchased from NatureWorks (Blair, NE, USA). Hydrolyzed PVA (MW: 78 KD) was purchased from Polysciences, Inc (Warrington, PA, USA). PMA (MW: 216 KD), Triton X-100 (p-tertiary-octyl polyethyl alchol), and Bovine Serum Albumin–fluorescein isothiocyanate conjugate were purchased from Sigma-Aldrich (St. Louise, MO, USA). 2-(N-morpholino)ethanesulfonic acid hemisodium salt (MES) was purchased from Sigma-Aldrich. Sulfo-NHS

and EDC were purchased from ThermoFisher Scientific (Rockford, IL, USA). Anhydrous Dimethylformamide (DMF) and phosphate buffered saline (PBS) salt were purchased from Sigma-Aldrich.

2.2 Formation of Electrospinning solutions

PLA was dissolved in DMF at 70 °C at 22 wt% PLA for at least an hour before spinning. PVA/PMA was prepared similar to methods from our previous work [4]. In summary, PVA was dissolved in deionized (DI) water and heat treated at 95 °C for 4 hours. PMA was also dissolved in DI-water and heat treated at 95 °C for 4 hours. The PVA/PMA solutions were mixed with mass ratio of PVA/PMA of 80/20 (*w/w*). Triton X-100 was added to the polymer solution to relieve surface tension. The mass ration of X-100/DI-water was 0.5/99.5 (*w/w*).

2.3 Electrospinning

PLA spinning dope was heated up to 70 °C. The solution was drawn into a 10 ml glass syringe. The spinning dope's temperature was maintained by a homemade ceramic heater that encapsulated the syringe. Additionally, a heat gun (Master Appliances Corp., Racine, WI, USA) heated the extrusion needle. A 21-gauge metal needle was used to extrude the polymer solution. A high voltage power source (Gamma High Voltage Research) supplied a 11 kV potential difference between the needle and a 3.5cm by 3.5cm copper collecting plate. The needle tip and plate were placed 10 cm apart. A programmable pump (Harvard Apparatus, Holliston, MA, USA) extruded polymer from the syringe at 10 uL/minute. Fibers were spun for 20 minutes. PVA/PMA dope was spun in a similar fashion. The dope was loaded into a plastic syringe and spun at room temperature. A 18 kV voltage was supplied, the distance from the needle tip to collector was 20 cm, and the solution feed rate was 0.5 ml/h. These NFs were spun for 3 hours.

2.4 Plasma Treatment

PE-100 Benchtop Plasma System (Plasma Etch, Carson City, NV, USA) was used for plasma treatment of PLA nanofibers. Oxygen plasma treatment was performed at 0.2 mbar pressure and 100, 200, and 300 watts for 3 minutes. The oxygen feed rate was 50 cc/minute.

2.5 Methylene Blue Dye Binding

A methylene blue dye binding assay was performed to estimate the carboxyl content of plasma treated PLA fabrics. Methylene blue dye has a single positive charge and should interact with carboxyl groups in a 1:1 molar fashion. For the experiment, a 20 mg/ml (ppm) methylene blue dye solution in DI-water is created. An equal volume of .1M borate buffer (pH = 8.4) is created and mixed with the dye solution (final concentration of 10 ppm). Each fabric piece ranging from 3 – 10 mg is placed in 10 ml of 10 ppm dye solution and incubated for 1 hour. After the incubation, supernatant from the fabric/dye solution was extracted and absorbance at 664 nm is taken to determine the amount of dye bound to the fabrics. This dye binding experiment was performed on untreated PLA, 100 watts, 200 watts, and 300 watt plasma treated PLA (3 minutes each). The results of the binding are normalized to mg of dye bound per gram of fabric.

2.6 Sulfo-NHS/EDC Chemistry

Plasma treated PLA NFs were incubated .1M Sulfo-NHS and .1M EDC in an MES buffer (pH = 5.4). The fabrics incubated for 90 minutes at room temperature before they were washed with a PBS solution. PVA/PMA fibers naturally produce carboxyl groups so sulfo-NHS/EDC chemistry can be done

on these fibers without any plasma modification.

2.7 Static BSA-FITC Binding

PLA fabrics that have been plasma activated (150 watts) and treated with sulfo-NHS/EDC chemistry were incubated in a .2 mg /ml BSA-FITC PBS (pH = 7.4) solution for 20 hours at ~8°C. Supernatant solution was obtained and absorbance at 494nm was measured using a PerkinElmer Lambda 35 UV/VIS spectrometer (Waltham, MA, USA) to determine the concentration of protein in the solution. Fabrics are then placed into filter holders and washed with pH 10 PBS at .2 ml/min for 50 minutes. Fabrics were then stored in the fridge at 4 °C until fluorescent images of the fibers could be obtained.

PVA/PMA fabrics had a different static adsorption. Fabrics were treated with sulfo-NHS/EDC chemistry and then incubated in .2 mg/ml BSA-FITC PBS (7.4) solution for 3 hours at room temperature (~21°C). Supernatant solution was obtained and absorbance at 494 nm was taken to determine the mass of protein bound to the fabrics. Fabrics were then placed in filter holders and washed with pH 10 PBS at .2 ml/min for 50 minutes. Fabrics were then stored in the fridge at 4°C until fluorescent images of the fibers could be obtained.

As inspired by Najafi et al. [4], Adsorption capacity (Q_p) will be defined as mg of protein bound per gram of fabric. This can be determined by the following equation:

$$Q_p = V \, (0.2 - C_s) \, / \, m$$

Were V being the volume (ml) of the protein solution the fabrics incubated in, C_s is the protein concentration (mg/ml) of the supernatant after the incubation period, and m is the mass (g) of the dry fabric.

2.8 Dynamic BSA-FITC Binding

PLA fabrics were additionally submitted to dynamic binding procedure. Sulfo-NHS/EDC treated fabrics were placed in filter holders and then had BSA-FITC solution run through them to initiate the covalent binding. .2 mg/ml BSA-FITC PBS solution was run through the fabrics at .05 ml/min for 1 hour. Fabrics were then washed with pH 10 PBS solution at .05 ml/min for 1 hour. The fabrics were then stored in the fridge at 4°C until fluorescent images could be obtained.

2.9 Confocal Fluorescent Imaging

The binding of BSA-FITC to the fibers was examined using a Zeiss 710 Confocal microscope (Carl Zeiss, Stockholm, Sweden). Fluorescent images were captured by using an excitation wavelength of 488nm and emission spectra of 510-530nm to produce the images. Some images have been enhanced using the contrast function on ImageJ™ open source software (National Institutes of Health, Bethesda, MD, USA).

3. Results and Discussion

3.1 Effectiveness of Plasma

Figure 3 shows the methylene blue dye binding capacity of PLA and plasma treated PLA at various voltages. According to the data, plasma treated fabrics bind significantly more methylene blue dye than non plasma treated fabrics. Considering the methylene blue interaction is electrostatic, it can be assumed that it is a negatively charged carboxyl group that is interacting with the positively charged dye molecule. It can also be seen that as one increases the energy of the plasma the amount of dye binding increases. This implies that higher energy plasma can create more carboxyl groups on the surface of the

NFs. The data shows that 200 watt plasma treatment raises the dye adsorption by more than 2 mg/g over 150 watt and 100 watt treatments. It should also be noted, that fabrics treated at higher plasma energy became more brittle and prone to fracture. This change in mechanical properties is likely due to increased chain breaking from the plasma treatment. Lastly, the chemical change cause by oxygen plasma treatment can be subjectively seen in figure 4. This image shows a plasma treated fabric that appears to be solvated in an aqueous solution compared to an untreated fabric that has maintained it hydrophobic character and floats on top of the solution.
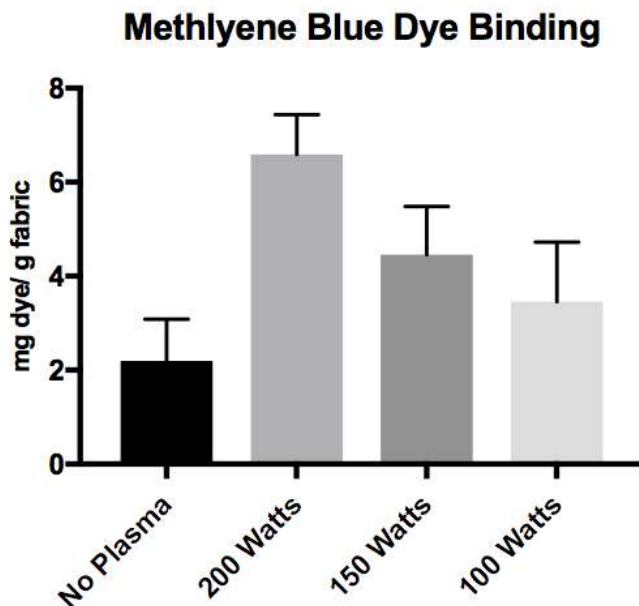

Figure 3. Carboxyl quantification of PLA NFs via methylene blue dye binding for various plasma treatment voltages for 3 minute treatment with 50 cc/min oxygen infusion.
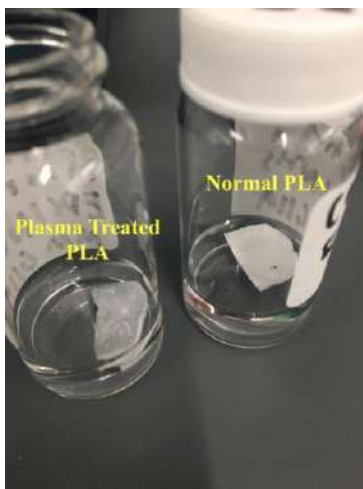
Figure 4. Image of plasma treated (left) and untreated PLA (right) fabrics in aqueous solutions
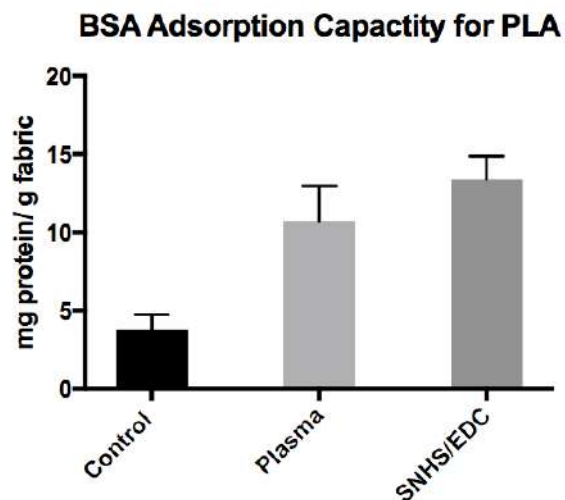
3.2 Static BSA-FITC Binding

   Quantitative results for BSA-FITC binding yielded peculiar results. Figure 5 implies that untreated PVA/PMA fibers bind more protein than fibers treated with sulfo-NHS/EDC chemistry. Clearly there is some significant nonspecific binding occurring likely due to PVA/PMA's ability to participate in hydrogen bonding. The reason for the discrepancy between the sulfo-NHS/EDC treated fabric and the control group may be due to a decrease in surface charge. As the sulfo-NHS/EDC reacts with fibers, it decreases the number of carboxyl groups that may be interacting with the protein. However, further experimentation is needed to explicitly determine the cause of the adsorption difference. As for PLA fabrics, Figure 6 shows that plasma treated and sulfo-NHS/EDC treated fabrics bound more protein than untreated PLA. There is no statistically significant difference between plasma treated fabrics and fabrics that had plasma and sulfo-NHS/EDC treatment. Because of this, we cannot determine whether any specific covalent binding is occurring. Qualitative data shows minimal differences in protein binding. Figure 7 shows fluorescent microscopy images of PVA/PMA fabrics under various treatments along with static binding procedure. Fibers can be seen in both however this is minimal if any difference in the brightness of the fabrics. This indicates a similar protein content on the surface of the fabrics. Similar results were seen for PLA fabrics (figure 8). The static binding method may not be optimal due to this high propensity for non-specific adsorption.
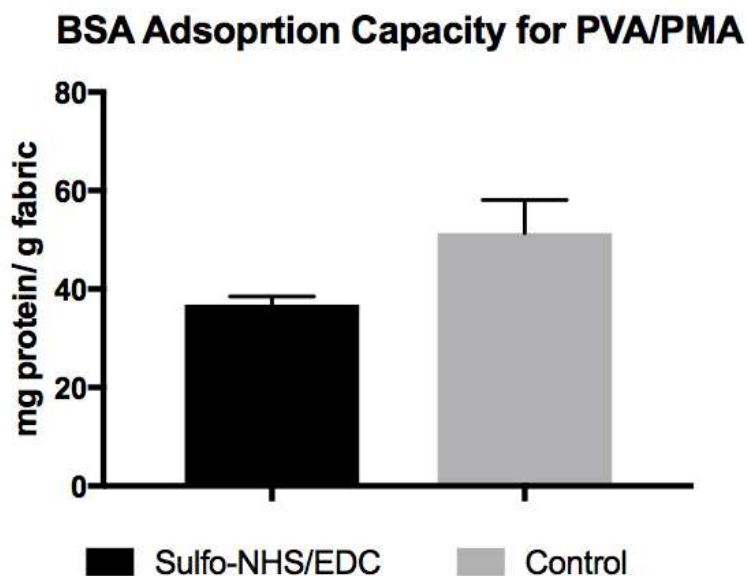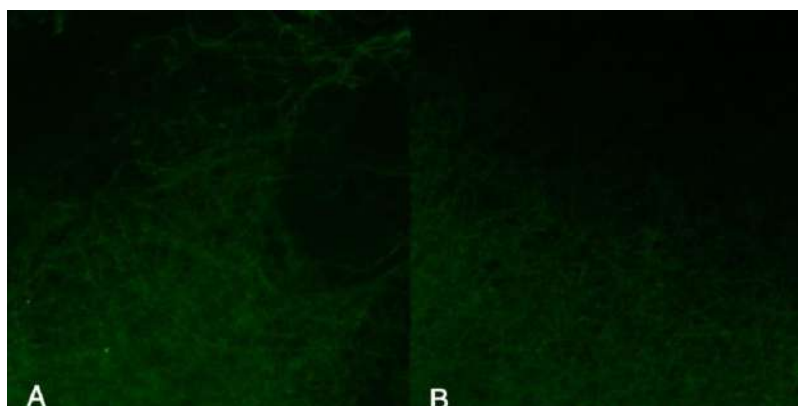

Figure 5. BSA-FITC Static Binding on PVA/PMA fibers treated with sulfo-NHS/EDC chemistry and control (untreated)

BSA Adsorption Capactity for PLA

Figure 6. BSA-FITC Static Binding on PLA fibers treated with plasma only (150 watt, 3 minutes), plasma and sulfo-NHS/EDC, and a control (untreated).

Figure 7. Confocal fluorescence images of PVA/PMA treated with sulfo-NHS/EDC (A) and untreated (B) after static BSA-FITC binding and PBS wash.
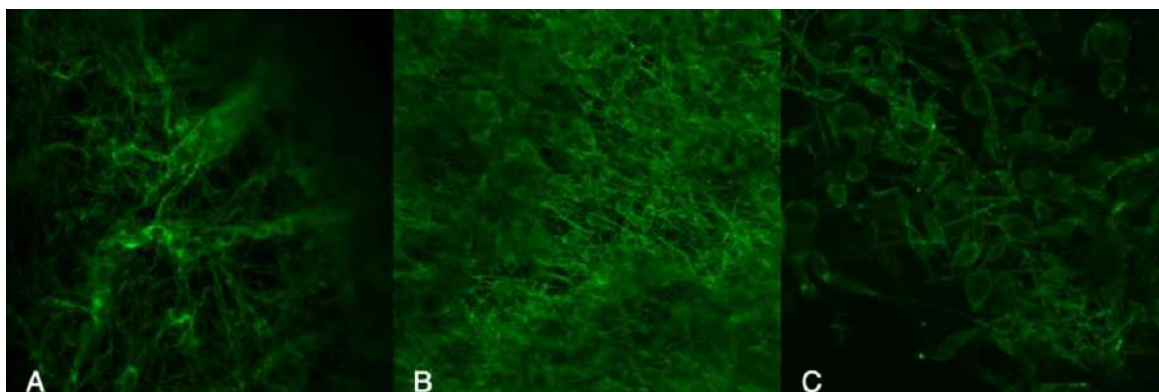
Figure 8. Confocal fluorescence images of PLA untreated (A), plasma treated (B), and treated with plasma and sulfo-NHS/EDC chemistry (C) after static BSA-FITC binding and PBS wash

3.3 Dynamic BSA-FITC Binding

The dynamic binding of BSA-FITC to PLA NFs appears to be more successful than both the static binding onto PVA/PMA and PLA. Specifically, the dynamic binding procedure provided bettered washing of nonspecifically bound protein and more specific covalent binding. This could be due to optimal washing conditions and minimization of nonspecific binding. Figure 9 shows that the PLA fabrics that receive sulfo-NHS/EDC treatment after plasma have brighter fibers than all of the other groups show. This is indicative of there being more protein bound on the fibers. Fibers can be seen in the other groups however this is likely baseline fluorescence noise from the fibers themselves. In the image of the PLA fibers that weren't treated with plasma, sulfo-NHS/EDC, or BSA-FITC, the fiber outlines can be seen. The images for plasma treated with BSA-FITC and untreated PLA with BSA-FITC show fibers that are no brighter than plain PLA. The additional green spots could be due to aggregated denatured protein or dust particles on the slides.
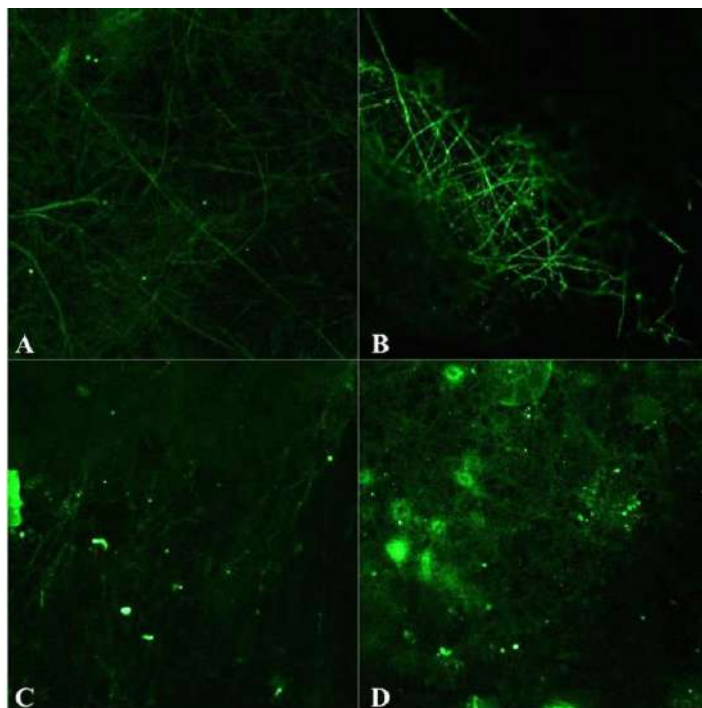
Figure 9. Confocal fluorescence images of PLA (A), PLA treated with plasma, sulfo-NHS, and dynamic BSA-FITC binding procedure (B), PLA treated with plasma and dynamic BSA-FITC binding procedure (C), and PLA treated only with dynamic BSA-FITC binding procedure (D).

4. Conclusion

In this work, covalently binding of proteins to various electrospun NFs was investigated. PLA NFs received oxygen plasma treatment to chemically modify the surface of the NFs. The data showed that dynamic binding of protein to PLA NFs with sulfo-NHS/EDC chemistry allowed for the covalent binding of proteins to the NFs. The dynamic binding method limited nonspecific adsorption better than the static binding method. Additionally, plasma treated PLA fibers showed increase carboxyl content which increased the hydrophilicity of the fibers. The increase in hydrophilicity allows for better diffusion of analytes dissolved in aqueous solution. This makes the fibers especially well suited for biosensor applications. PVA/PMA fibers appear to have a high level of non-specific adsorption with the protein and may need additional modification to limit this key flaw before these fibers can used in practical

applications. Future studies could be performed to optimize the covalent binding of protein while limiting nonspecific adsorption. Different solution feed rates for dynamic protein binding could be explored as well as different washing conditions. Additionally, experiments could be run to determine why static binding increases nonspecific adsorption relative to the dynamic binding. The results of this project present a material that can be used in a variety of applications. The enhanced PLA fibers could be applied to increase sensitivity and reliability of biosensors and create protein functionalized tissue engineering scaffolds.

References

1) Prabhu, P. Nanofibers for Medical Diagnosis and Therapy Handbook of Nanofibers. 2018, 1-37 DOI: 10.1007/978-3-319-42789-8_48-1

2) Mahmoudifard, M.; Soudi, S.; Soleimani, M.; Hosseinzadeh, S.; Esmaeili, E.; Vossoughi, M. Efficient protein immobilization on polyethersolfone electrospun nanofibrous membrane via covalent binding for biosensing applications *Mater Sci Eng C Mater Biol Appl* **2016**, 58, 586-94 DOI: 10.1016/j.msec.2015.09.007

3) Sapountzi, E.; Braiek, M.; Chateaux, J. F.; Jaffrezic-Renault, N.; Lagarde, F. Recent Advances in Electrospun Nanofiber Interfaces for Biosensing Devices *Sensors* **2017**, 17, 1887 DOI: 10.3390/s17081887

4) Najafi, M.; Chery, J.; Frey, M.W. Functionalized Electrospun Poly(Vinyl Alcohol) Nanofibrous Membranes with Poly(Methyl Vinyl Ether-Alt-Maleic Anhydride) for Protein Adsorption *Materials* **2018**, 11(6), 1002 DOI:10.3390/ma11061002

5) Kim, D.; Herr, A.E. Protein immobilization techniques for microfluidic assays *Biomicrofluidics* **2013**, 7(4):041501 DOI: 10.1063/1.4816934

6) Jacobs, T.; Declercq, H.; De Geyter, N.; Cornelissen, R.; Dubruel, P.; Leys, C.; Beaurain, A.; Payen, E.; Morent, R. Plasma surface modification of polylactic acid to promote interaction with fibroblasts *J Mater Sci Mater Med* **2013**, 24(2), 469-78 DOI: 10.1007/s10856-012-4807-z

7) Chen, J.P.; Su, C.H. Surface modification of electrospun PLLA nanofibers by plasma treatment and cationized gelatin immobilization for cartilage tissue engineering *Acta Biomater* **2011**, 7(1), 234-43 DOI:10.1016/j.actbio.2010.08.015

8) Xia, Y.; Boey, F.; Venkatraman, S.S. Surface modification of poly(L-lactic acid) with biomolecules to promote endothelialization *Biointerphases* **2010**, 5(3), 32-40 DOI: 10.1116/1.3467508

9) Paletta, J.R.; Bockelmann, S.; Walz, A.; Theisen, C.;, Wendorff, J.H.; Greiner, A.; Fuchs-Winkelmann, S.; Schofer, M.D. RGD-functionalisation of PLLA nanofibers by surface coupling using plasma treatment: influence on stem cell differentiation *J Mater Sci Mater Med* **2010**, 21(4), 1363-9 DOI: 10.1007/s10856-009-3947-2

10) Reinholt, S.J.; Sonnenfeldt, A.; Naik, A.; Frey, M.W.; Baeumner, A.J. Developing new materials for paper-based diagnostics using electrospun nanofibers *Anal Bioanal Chem* **2014**, 406(14), 3297-304 DOI: 10.1007/s00216-013-7372-5

11) Matlock-Colangelo, L.; Coon, B.; Pitner, C.L.; Frey, M.W.; Baeumner, A.J. Functionalized electrospun poly(vinyl alcohol) nanofibers for on-chip concentration of E. coli cells *Anal Bioanal Chem* **2016**, 408(5), 1327-34 DOI: 10.1007/s00216-015-9112-5

12) Vashist, S.K. Comparison of 1-Ethyl-3-(3-Dimethylaminopropyl) Carbodiimide Based Strategies to Crosslink Antibodies on Amine-Functionalized Platforms for Immunodiagnostic Applications *Diagnostics* **2012**, 2(3), 22-33 DOI: 10.3390/diagnostics2030023

13) Bartczak, D.; Kanaras, A.G. Preparation of Peptide-Functionalized Gold Nanoparticles Using One Pot EDC/Sulfo-NHS Coupling *Langmuir* **2011**, 27(16), 10119-23 DOI: 10.1021/la2022177

14) Ikada, Y.; Tsuji, H. Biodegradable polyesters for medical and ecological applications *Macromol. Rapid Commun.* **2000**, 21(3), 117-32 DOI: 10.1002/(SICI)1521-3927(20000201)21

15) González, E.; Sheperd, L.M.; Saunders, L.; Frey, M.W. Surface Functional Poly(lactic Acid)

Electrospun Nanofibers for Biosensor Applications *Materials* **2016**, 9(1), 47 DOI: 10.3390/ma9010047

16) Narayanan, N.; Jiang, C.; Uzunalli, G.; Thankappan, S.K.; Laurencin, C.T.; Deng, M. Polymeric Electrospinning for Musculoskeletal Regenerative Engineering *Regen. Eng. Transl. Med.* **2016**, 2, 69-84 DOI: 10.1007/s40883-016-0013-8

Synthesis of Block Copolymer with Mixed Electronic-Ionic Conductivity

Meg Tetzloff[1,2], Ziwei Liu[2], Christopher Ober[2]

[1]Department of Chemical Engineering, Michigan Technological University, Houghton, MI
[2]Department of Materials Science and Engineering, Cornell University, Ithaca, NY

ABSTRACT: Copolymers with blocks that exhibit electronic and ionic conductivity have been discovered to be useful for energy harvesting storage, such as in batteries, sensor, etc. However, the current conductivities exhibited by these organic batteries do not rival those of standard batteries. This project has explored the effect of linking various lengths of the ionically conductive poly(di(ethylene glycol) methyl ether methacrylate) homopolymer to a fixed length electronically conductive poly(3-hexylthiophene) homopolymer to determine the optimal ratio between blocks for self-assembly and highest conductivity.

I. INTRODUCTION

Linking immiscible well-defined polymer blocks with covalent bonds to simultaneously utilize the properties of each block is useful in developing highly engineered materials. A benefit of block copolymers with immiscible blocks is their ability to self-assemble into phase-separated morphologies, so that the blocks align and do not hinder the properties of the other block.[1]

The conjugated regioregular polymer poly(3-hexylthiophene) (P3HT) is an electrically conductive material has been the subject of significant research in recent years due to its use as a flexible organic semiconductor, with current applications including organic photovoltaic cells, light-emitting diodes, and field-effect transistors.[2,3]

Polymers with a high density of ethylene oxide have been found to be ionically conductive.[4] The polymer poly(di(ethylene glycol) methyl ether methacrylate) (PDEOMEMA) is one such molecule that can be synthesized with a good control of molecular weight and polydispersity using atom transfer radical polymerization (ATRP).[5]

By combining the electronically conductive properties of P3HT with the ionically conductive PDEOMEMA, a block copolymer can be formed that is useful in batteries, which require both of these properties. While a typical battery contains an electrolyte for ion transport and electrodes for electronic conduction, an ordered block copolymer can serve both these functions in a single material that is low-cost, lightweight, and flexible.[6]

The goal of this project is to link a fixed-length P3HT block (with a molecular weight of 8,000) to a variable-length PDEOMEMA block with "click" chemistry in order to optimize the ratio of electronic conductivity to ionic conductivity. This will allow the development of organic batteries with higher conductivities. Creating a PDEOMEMA block with a polydispersity index (PDI) of below 1.4 will allow us to create a uniform

material and more accurately analyze the effect of the chain length on conductivity.

II. EXPERIMENTAL

ATRP of PDEOMEMA Block

Because of the oxygen sensitivity of the copper catalyst required for ATRP, the reaction needs to occur in an oxygen free environment. In a Schlenk flask, 2-azidoethyl 2-bromo-2-methylpropanoate initiator (1 molar equivalent), di(ethylene glycol) methyl methacrylate (DEOMEMA) monomer (100 molar equivalents for ATRP 1, 3-5; 200 equivalents for ATRP 2) and Fisher Brand anhydrous ethanol were added and the flask was sealed with a rubber septum. Five freeze-pump-thaw cycles were completed and the flask was purged with argon. Cu(I)Br activator (1 molar equivalent) and 2,2'-bipyridine ligand (2 molar equivalents equivalents) were weighed into a second Schlenk flask containing a magnetic stir bar and fitted with a rubber septum. The flask was degassed and purged with argon five times. A cannula transfer was used to transport the contents of the first flask into the second flask. This mixture was stirred in a 60 ℃ oil bath for varied amounts of time to produce PDEOMEMA polymers of different molecular weights. Variable reaction conditions are summarized in Table 1. The reaction was quenched by opening the flask and allowing air to oxidize the Cu(I) catalyst.

Purification of PDEOMEMA

A 25 mL syringe of neutral alumina was used as a column to remove the copper from the reacted solution. The solution was diluted with THF and allowed to pass through the column, and the THF was removed by rotary evaporation. To further purify the polymer, the solution was placed in a 3.5k MWCO membrane for dialysis and stirred in anhydrous ethanol for 24 hours to remove unreacted monomer, initiator, and ligand. The solution was then transferred from the membrane to a flask, and ethanol was removed by rotary evaporation and vacuum oven. The polymer was then characterized with Gel Permeation Chromatography (GPC) and Fourier Transform Infrared Spectroscopy (FTIR) analysis.

Deprotection of P3HT Block

The previously prepared P3HT polymer was functionalized with an alkyne end group for use in the click reaction. To keep this alkyne group from reacting with itself in the presence of oxygen, it had been protected with a trimethylsilyl (TMS) group. To remove this group, the molecule was dissolved in anhydrous THF and stirred with 5 molar equivalents of tetra-n-butylammonium fluoride (TBAF) in a flask at room temperature for 2 hours. A rotary evaporator was used to remove the THF. The deprotected P3HT polymer was then precipitated with methanol and filtered gravimetrically, then dried in a vacuum oven.

Azide-Alkyne "Click" Reaction

One molar equivalent of P3HT, 1 molar equivalent of PDEOMEMA, and 2 molar equivalents of N,N,N′,N″,N″-pentamethyldiethylenetriamine (PMDETA)

Table 1*: ATRP molecular weight data.*
ATRP 3 yielded no results in GPC analysis likely because it was lost through the dialysis membrane.

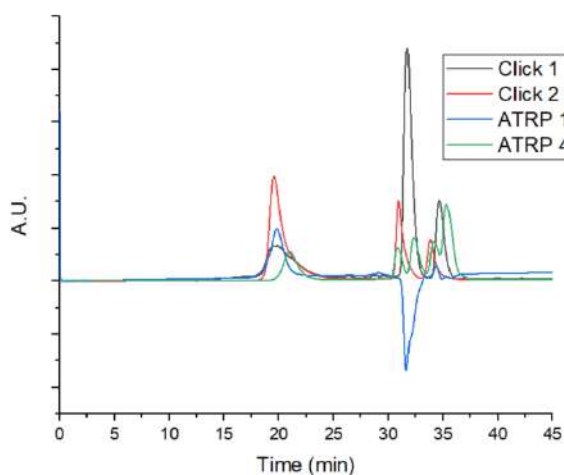| ATRP	Reaction Time (hr)	Initiator : Monomer	M_n	PDI
1	21	1:100	18,000	1.18
2	21	1:200	16,000	1.14
3	4	1:100	-	-
4	8	1:100	8,000	1.12
5	26	1:100	24,000	1.86

ligand were dissolved in anhydrous THF and bubbled with argon for 30 minutes. In a Schlenk flask containing a magnetic stir bar, 2 equivalents of CuI catalyst were degassed and purged with argon five times. A cannula transfer was used to transport the contents of the first flask into the second, and the mixture was stirred in a 40 ºC oil bath for 72 hours.

Purification of P3HT-b-PDEOMEMA

As with the purification of the PDEOMEMA block, a 25 mL syringe of neutral alumina was used as a short column to remove the copper from the solution. The polymer was diluted in THF and passed through the syringe and collected in a flask. The flask was then rotary evaporated to remove the THF, and the polymer was precipitated in methanol. A vacuum pump was then used to dry the polymer. GPC and FTIR were used to analyze the polymer.

III. RESULTS

Five homopolymer blocks of PDEOMEMA were synthesized, and two were considered feasible for testing as a unique block for the copolymer. ATRP 1 and 4 were used because of their widely different molecular weights, their consistency in ratio of reactants, and their sufficiently low polydispersities. The GPC curves can be found in Figure 1 while the molecular weight data for the click reactions can be found in Table 2.

Table 2: Click reaction molecular weight data

Click Reaction	ATRP Used	Reaction Time (hr)	M_n	PDI
1	1	72	14,000	1.36
2	4	72	14,000	1.38

a.)

b.)
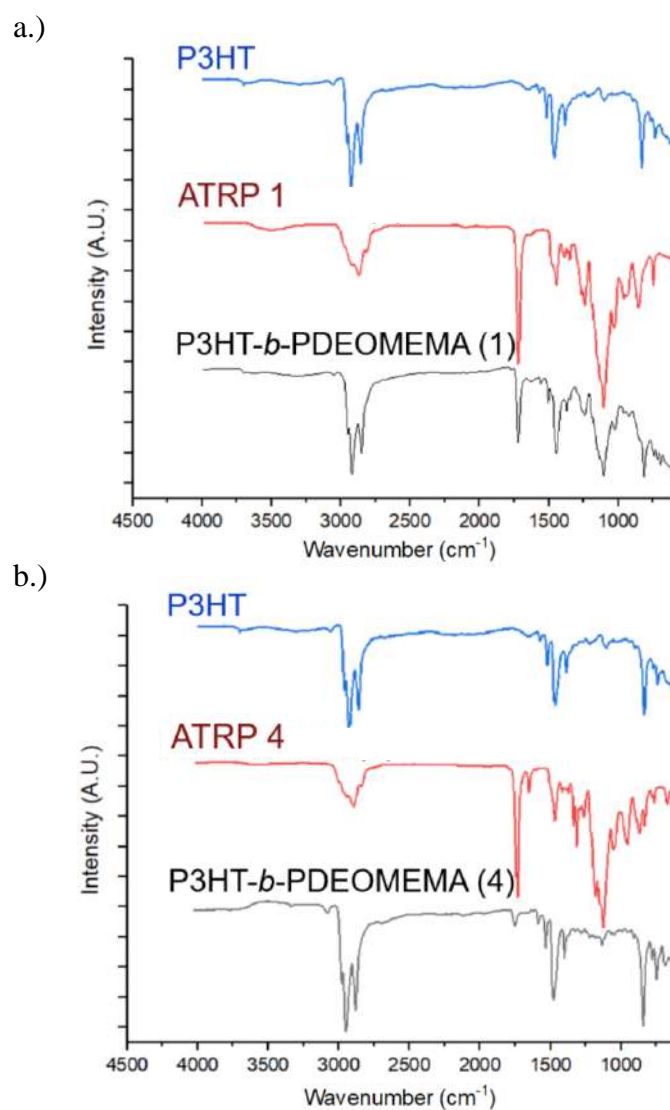
Figure 2: FTIR data. a.) Comparison of P3HT and ATRP 1 blocks to P3HT-b-PDEOMEMA (1); b.) Comparison of P3HT and ATRP 4 blocks to P3HT-b-PDEOMEMA (4)

Figure 1: GPC curves for PDEOMEMA polymers and P3HT-b-PDEOMEMA copolymers

IV. DISCUSSION

The GPC and FTIR results confirm the synthesis of the P3HT-*b*-PDEOMEMA copolymer. While the GPC results for the block copolymer report lower molecular weight averages than one might predict by adding the average molecular weights of each block, the average molecular weight reported was likely skewed to be lower than the weight of the copolymer due to the existence of unreacted homopolymers in the sample.

The carbonyl group present in the PDEOMEMA homopolymer can be seen in both FTIR graphs in the strong peak around 1750 cm^{-1}. This peak is also present in both block copolymers, which confirms the presence of the PDEOMEMA block. Because the polymer was also able to be precipitated in methanol, we are able to confirm that the P3HT block is present in the macromolecule, because P3HT precipitates in methanol while PDEOMEMA does not. This information coupled suggests that a P3HT-*b*-PDEOMEMA copolymer was synthesized.

To fully test a range of ratios of the two polymer blocks, additional lengths of PDEOMEMA polymers need to be synthesized, especially in molecular weights less than that of the P3HT block, and slightly larger than the P3HT block. In order to purify PDEOMEMA polymers with lower molecular weights, a dialysis membrane with smaller pores is necessary.

In order to analyze the effectiveness of these block copolymers, future analysis needs to be completed. It is important to optimize the electronic and ionic conductivities of the polymer, so both should be taken into account when analyzing the effects of the PDEOMEMA chain length. Atomic force microscopy can determine the morphology of a spin-coated sample. A well-ordered structure would suggest formation of nanopathways for effective charge transport, while a disordered morphology would likely hinder both conductivities.

V. CONCLUSION

Two block copolymers of P3HT and varied lengths of PDEOMEMA were synthesized and characterized with GPC and FTIR analysis. While the conductive and morphological properties of the polymer have not yet been measured, the work done on this project shows potential to create optimized polymers with simultaneous ionic-electronic conductivity that can be useful in solid organic batteries.

VI. ACKNOWLEDGEMENTS

VII. REFERENCES

1. Javier, A. E., Patel, S. N., Hallinan, D., Srinivasan, V., Balsara, N. P. Simultaneous Electronic and Ionic Conduction in a Block Copolymer: Application in Lithium Battery Electrodes. *Angewandte Chemie*, **2011**, 42, 10022–10025.

2. P. C. Ewbank, D. Laird, R. D. McCullough in Organic Photovoltaics, Wiley-VCH, **2009**, 1 – 55.

3. Obrzut, Jan, and Kirt A. Page. Electrical Conductivity and Relaxation in Poly(3-Hexylthiophene). *Physical Review B*, **2009**, 80.

4. Berthier, C., Gorecki, M., Armand, M. B., Chabagno, J. M., Rigaud, P. Microscopic investigation of ionic conductivity in alkali metal salts-poly(ethylene oxide) adducts. *Solid State Ionics* **11**, 91–96 (1983).

5. Young, R. J.; Lovell, P. A. *Introduction to Polymers, 3rd ed.*; CRC Press: Boca Raton, 2011

6. Gu, Z., Kanto, T., Tsuchiya, K., Shimomura, T., Ogino, K. Annealing Effect on Performance and Morphology of Photovoltaic Devices Based on Poly(3-Hexylthiophene)-b-Poly(Ethylene Oxide). *Journal of Polymer Science Part A: Polymer Chemistry*, **2011**, 49, 2645–2652.

A Comparison of Mapping Variable and Coherent State Instantons

Peter Tomlinson, Binghamton University
Srinath Ranya, Ananth Lab, Cornell University

Abstract

Mapping variable and coherent state ring polymers are two representations of the path integral discretization of the quantum partition function, which take into account diabatic states. This allows for the study of chemical reactions in the non-adiabatic limit. Both methods use the standard ring polymer path integral representation for nuclear variables, and map discrete states to continuous electronic variables. Python code was written to determine the instanton for the coherent state method, and compared to the mapping variable instanton. Although each are exactly defined, with similar procedures for computing the instanton, the coherent state results were inconsistent with the mapping variable results.

1 Introduction

Quantum mechanics provides an accurate picture of nature on its smallest scale, but quantum calculations are computationally expensive. It is only feasible to exactly model the simplest of systems. Quantum calculations scale exponentially with the the number of variables, whereas classical calculations scale linearly. Therefore, if an analogous classical formulation can capture quantum phenomena, a quantum system's dynamics may be modeled approximately. Its statistics are modeled exactly.
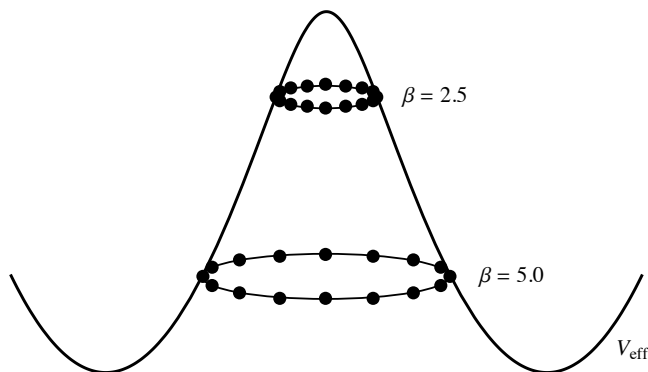
Ring Polymer Molecular Dynamics (RPMD) is one approach developed to study nuclear dynamics and quantum effects such as tunneling. In this formulation, path integral discretization creates N identical copies of a particle, called beads, connected in a ring by springs. This ring polymer simulates tunneling by draping over or wrapping around a potential barrier, similarly to what is shown in figure 1. At higher temperatures and therefore higher energies, the ring polymer contracts and will collapse to a single classical point resting on the potential surface. Modeling the classical trajectory of each bead determines the reaction rate and transition state of a reaction. Specifically, figure 1 illustrates a pair of instantons, which represent the dominant tunneling pathways. [1]

RPMD is an established method for one state systems. [2] It is therefore well suited for adiabatic systems, such as the one shown in figure 2, where the reaction may be approximated to occur on one surface. Mapping variable [3] and coherent state [4] ring polymer molecular dynamics (MV-RPMD and CS-RPMD respectively) are recently developed methods for applying the path integral formalism to multiple state systems. They therefore allow for the study of systems in the non-adiabatic limit. Thus, they show potential for multi-electron reactions, such as in photochemistry. [3] This report compares the derivation and instantons of the mapping variable and coherent state methods.

Figure 1: Diagram of ring polymer instantons simulating tunneling through a potential barrier at low temperature ($\beta = 5.0$) and at high temperature ($\beta = 2.5$)
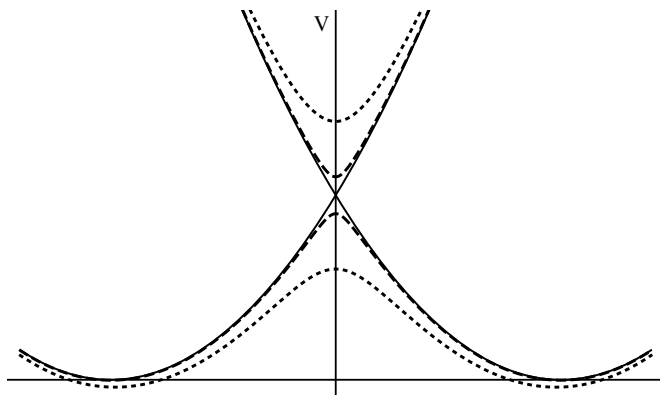

Figure 2: Diabatic states are given by the solid lines, states with weak coupling, in the non-adiabatic limit, are given by the dashed lines, and states with strong coupling, in the adiabatic limit, are given by the dotted lines

2 Theory

2.1 The Path Integral Ring Polymer

The Hamiltonian for a general L-level system is given as

$$\hat{H} = \frac{\hat{\mathbf{P}}^2}{2M} + V_0(\hat{\mathbf{R}}) + \sum_{n,m=1}^{L} V_{nm}(\hat{\mathbf{R}})|n\rangle\langle m|, \qquad (1)$$

where $\mathbf{R}$ and $\mathbf{P}$ denote the nuclear position and momentum, M is the nuclear mass, $V_0(\mathbf{R})$ is the electronic state-independent potential, $V_{nn}(\mathbf{R})$ is the potential for the nth electronic state, and $V_{nm}(\mathbf{R})$ for $n \neq m$ is the coupling between electronic states. The electronic state potential energy will later be denoted as $\mathcal{V}(\mathbf{R})$ for simplicity.

We begin the derivation of the ring polymer Hamiltonian with the canonical quantum partition function, given as

$$Z = \text{Tr}\left[e^{-\beta\hat{H}}\right], \qquad (2)$$

where $\beta = 1/k_B T$ is the reciprocal temperature. β can also be interpreted as imaginary time, since the transformation $\beta = it/\hbar$ corresponds to a Wick rotation from the canonical density matrix $\hat{\rho}(t) = \exp[-\beta\hat{H}]$ to the time evolution operator $\hat{U}(t) = \exp[-i\hat{H}t/\hbar]$. [2] Using the Trotter expansion,

$$e^{-\beta\hat{H}} = \lim_{N\to\infty}[e^{-\beta_N \frac{\hat{\mathbf{P}}^2}{2M}}e^{-\beta_N \hat{V}_0(\hat{\mathbf{R}})}e^{-\beta_N \mathcal{V}(\hat{\mathbf{R}})}]^N, \qquad (3)$$

where $\beta_N = \beta/N$. Using equation (3) and writing out the trace, the partition function becomes

$$Z = \lim_{N\to\infty}\int d\mathbf{R}\int d\mathbf{x}$$
$$\langle \mathbf{R}, \mathbf{x}|[e^{-\beta_N \frac{\hat{\mathbf{P}}^2}{2M}}e^{-\beta_N \hat{V}_0(\hat{\mathbf{R}})}e^{-\beta_N \mathcal{V}(\hat{\mathbf{R}})}]^N|\mathbf{R}, \mathbf{x}\rangle, \qquad (4)$$

where $\mathbf{x}$ and $\mathbf{p}$ are introduced as electronic position and momentum.

According to the path integral procedure, the identity $\hat{I} = \int d\mathbf{R}\int d\mathbf{x}|\mathbf{R}, \mathbf{x}\rangle\langle \mathbf{R}, \mathbf{x}|$ is inserted into equation (4) $N-1$ times, yielding

$$Z = \lim_{N\to\infty}\int d\{\mathbf{R}_\alpha\}\int d\{\mathbf{x}_\alpha\}$$
$$\prod_{\alpha=1}^{N}\langle \mathbf{R}_\alpha|e^{-\frac{\beta_N}{2M}\hat{\mathbf{P}}^2}|\mathbf{R}_{\alpha+1}\rangle e^{-\beta_N V_0(\mathbf{R}_\alpha)}$$
$$\langle \mathbf{x}_\alpha|e^{-\beta_N \mathcal{V}(\mathbf{R}_\alpha)}|\mathbf{x}_{\alpha+1}\rangle. \qquad (5)$$

The notation $\int d\{\mathbf{R}_\alpha\}$ represents $\int d\mathbf{R}_1 \int d\mathbf{R}_2 \cdots \int d\mathbf{R}_N$. Note that because of the initial trace, $\mathbf{R}_1 = \mathbf{R}_{N+1}$ and $\mathbf{x}_1 = \mathbf{x}_{N+1}$. Now the $\hat{\mathbf{P}}$ term in equation (5) can be evaluated by inserting $\hat{I} = \int d\mathbf{P}|\mathbf{P}\rangle\langle \mathbf{P}|$, and the nuclear momentum is introduced using the Gaussian integral

$$\int d\{\mathbf{P}_\alpha\}\prod_{\alpha=1}^{N}e^{-\beta_N \mathbf{P}_\alpha^2/2M} = \left(\frac{2\pi M}{\beta_N}\right)^{N/2}. \qquad (6)$$

Also, throughout this report we set $\hbar = 1$.

The partition function is evaluated as

$$Z \propto \lim_{N\to\infty}\int d\{\mathbf{R}_\alpha\}\int d\{\mathbf{P}_\alpha\}e^{-\beta_N H_{RP}}I_E \qquad (7)$$

where

$$H_{RP} = \sum_{\alpha=1}^{N}\frac{\mathbf{P}_\alpha^2}{2M} + V_0(\mathbf{R}_\alpha) + \frac{M}{2\beta_N^2}(\mathbf{R}_\alpha - \mathbf{R}_{\alpha+1})^2 \qquad (8)$$

and

$$I_E = \int d\{\mathbf{x}_\alpha\}\prod_{\alpha=1}^{N}\langle \mathbf{x}_\alpha|e^{-\beta_N \mathcal{V}(\mathbf{R}_\alpha)}|\mathbf{x}_{\alpha+1}\rangle. \qquad (9)$$

H_{RP} is an established result of the Path Integral Ring Polymer method for single state systems. [2] MV-RPMD [3] and CS-RPMD [4] have been developed to handle multiple state systems, and differ in the way they handle I_E.

2.2 Mapping Electronic States

The Stock-Thoss mapping representation [5] is used in both MV-RPMD and CS-RPMD to be able to express the discrete electronic states in terms of continuous phase space variables $\mathbf{x}$ and $\mathbf{p}$. Under this protocol, L diabatic electronic states $|\psi\rangle$ are mapped to L singly excited harmonic oscillators (SEOs), such that

$$|\psi_n\rangle\langle\psi_m| \to \hat{a}_n^\dagger \hat{a}_m \qquad (10)$$

and

$$|\psi_n\rangle \to |0_1, \ldots, 1_n, \ldots, 0_L\rangle = |n\rangle. \qquad (11)$$

In this notation, $|n\rangle$ is the product of L oscillators with the nth in first excited state and the remainder in the ground state. The terms $\hat{a}_n^\dagger$ and $\hat{a}_m$ are the harmonic oscillator creation and annihilation operators respectively, they are given by

$$\hat{a}_n^\dagger = \frac{\hat{x}_n - i\hat{p}_m}{\sqrt{2}} \quad \text{and} \quad \hat{a}_m = \frac{\hat{x}_m + i\hat{p}_m}{\sqrt{2}}, \qquad (12)$$

and obey the commutation rule $[\hat{a}_n^\dagger, \hat{a}_m] = \delta_{nm}$.

The projection of an SEO state onto an electronic position state is given by

$$\langle \mathbf{x}|n\rangle = \frac{\sqrt{2}}{\pi^{N/4}}[\mathbf{x}]_n e^{-\frac{1}{2}\mathbf{x}^2}. \qquad (13)$$

Coherent states, denoted $|\mathbf{p}, \mathbf{q}\rangle$ are eigenstates of the annihilation operator. Here, $\mathbf{q}$ represents the electronic position, and is equivalent to $\mathbf{x}$. The projection of an SEO state onto a coherent state is found as

$$\langle \mathbf{p}, \mathbf{q}|n\rangle = \langle \mathbf{p}, \mathbf{q}|\hat{a}_n^\dagger|0\rangle = \frac{q_n - ip_n}{\sqrt{2}}\langle \mathbf{p}, \mathbf{q}|0\rangle$$
$$= \frac{q_n - ip_n}{\sqrt{2}}\int_{-\infty}^{\infty}dx\langle \mathbf{p}, \mathbf{q}|x\rangle\langle x|0\rangle \qquad (14)$$
$$= \frac{q_n - ip_n}{\sqrt{2}}e^{-\frac{1}{4}(\mathbf{q}^2+\mathbf{p}^2)},$$

Likewise

$$\langle m|\mathbf{p}, \mathbf{q}\rangle = \langle 0|\hat{a}_m|\mathbf{p}, \mathbf{q}\rangle = \frac{q_m + ip_m}{\sqrt{2}}\langle 0|\mathbf{p}, \mathbf{q}\rangle$$

$$= \frac{q_m + ip_m}{\sqrt{2}} \int_{-\infty}^{\infty} dx\langle 0|x\rangle\langle x|\mathbf{p}, \mathbf{q}\rangle \qquad (15)$$

$$= \frac{q_m + ip_m}{\sqrt{2}} e^{-\frac{1}{4}(\mathbf{q}^2 + \mathbf{p}^2)}.$$

2.3 Mapping Variable Ring Polymer

MV-RPMD expresses I_E in phase space by applying Wigner transforms. The Wigner function is given by

$$O(\mathbf{x}, \mathbf{p}) = \int d\Delta\mathbf{x}\left\langle \mathbf{x} - \frac{\Delta\mathbf{x}}{2}\middle|\hat{O}\middle|\mathbf{x} + \frac{\Delta\mathbf{x}}{2}\right\rangle e^{i\mathbf{p}^T\Delta\mathbf{x}} \qquad (16)$$

and is used to find the trace of an operator in phase space,

$$\mathrm{Tr}[\hat{O}] = \frac{1}{(2\pi)^L} \int d\mathbf{x} \int d\mathbf{p}\, O(\mathbf{x}, \mathbf{p}). \qquad (17)$$

First, to ensure the projection onto the SEO subspace, insert the diabatic projection operator $\mathcal{P} = \sum_n |n\rangle\langle n|$ throughout I_E,

$$I_E = \int d\{\mathbf{x}_\alpha\} \prod_{\alpha=1}^{N} \langle\mathbf{x}_\alpha|\mathcal{P}e^{-\beta_N\mathcal{V}(\mathbf{R}_\alpha)}\mathcal{P}|\mathbf{x}_{\alpha+1}\rangle. \qquad (18)$$

Now, if we define

$$\hat{S} = \mathcal{P}e^{-\beta_N\mathcal{V}(\mathbf{R}_1)}\mathcal{P}|\mathbf{x}_2\rangle\langle\mathbf{x}_2|\mathcal{P}e^{-\beta_N\mathcal{V}(\mathbf{R}_2)}\mathcal{P}|\mathbf{x}_3\rangle$$
$$\cdots \langle\mathbf{x}_N|\mathcal{P}e^{-\beta_N\mathcal{V}(\mathbf{R}_N)}\mathcal{P}, \qquad (19)$$

we can write I_E as a trace of $\hat{S}$ over $\mathbf{x}_1$,

$$I_E = \int d\mathbf{x}_2 \cdots \int d\mathbf{x}_N \, \mathrm{Tr}[\hat{S}]_1. \qquad (20)$$

Applying equations (16) and (17), I_E becomes

$$I_E = \frac{1}{(2\pi)^L} \int d\mathbf{x}_1 \int d\mathbf{p}_1 \int d\Delta\mathbf{x}_1 \int d\mathbf{x}_2 \cdots \int d\mathbf{x}_N$$
$$\left\langle \mathbf{x}_1 - \frac{\Delta\mathbf{x}_1}{2}\middle|\hat{S}\middle|\mathbf{x}_1 + \frac{\Delta\mathbf{x}_1}{2}\right\rangle e^{i\mathbf{p}_1^T\Delta\mathbf{x}_1}. \qquad (21)$$

By rearranging I_E as

$$I_E = \frac{1}{(2\pi)^L} \int d\mathbf{x}_1 \int d\mathbf{p}_1 \int d\Delta\mathbf{x}_1 \int d\mathbf{x}_2 \cdots \int d\mathbf{x}_N$$

$$\langle\mathbf{x}_2|\mathcal{P}e^{-\beta_N\mathcal{V}(\mathbf{R}_2)}\mathcal{P}|\mathbf{x}_3\rangle \cdots \langle\mathbf{x}_N|\mathcal{P}e^{-\beta_N\mathcal{V}(\mathbf{R}_N)}\mathcal{P}|\mathbf{x}_1 + \frac{\Delta\mathbf{x}_1}{2}\rangle$$

$$\langle\mathbf{x}_1 - \frac{\Delta\mathbf{x}_1}{2}|\mathcal{P}e^{-\beta_N\mathcal{V}(\mathbf{R}_1)}\mathcal{P}|\mathbf{x}_2\rangle e^{i\mathbf{p}_1^T\Delta\mathbf{x}_1}, \qquad (22)$$

and redefining $\hat{S}$ as

$$\hat{S} = \mathcal{P}e^{-\beta_N\mathcal{V}(\mathbf{R}_2)}\mathcal{P}|\mathbf{x}_3\rangle \cdots \langle\mathbf{x}_N|\mathcal{P}e^{-\beta_N\mathcal{V}(\mathbf{R}_N)}\mathcal{P}|\mathbf{x}_1 + \frac{\Delta\mathbf{x}_1}{2}\rangle$$

$$\langle\mathbf{x}_1 - \frac{\Delta\mathbf{x}_1}{2}|\mathcal{P}e^{-\beta_N\mathcal{V}(\mathbf{R}_1)}\mathcal{P}, \qquad (23)$$

I_E can be written as

$$I_E = \int d\mathbf{x}_1 \int d\mathbf{p}_1 \int d\Delta\mathbf{x}_1$$
$$\int d\mathbf{x}_3 \cdots \int d\mathbf{x}_N \, \mathrm{Tr}[\hat{S}]_2 \, e^{i\mathbf{p}_1^T\Delta\mathbf{x}_1}, \quad (24)$$

and equations (16) and (17) can again be applied. Repeating this process a total of N times yields

$$I_E = \frac{1}{(2\pi)^{LN}} \int d\{\mathbf{x}_\alpha\} \int d\{\mathbf{p}_\alpha\} \int d\{\Delta\mathbf{x}_\alpha\}$$

$$\prod_{\alpha=1}^{N} \left\langle \mathbf{x}_\alpha - \frac{\Delta\mathbf{x}_\alpha}{2}\middle|\mathcal{P}e^{-\beta_N\mathcal{V}(\mathbf{R}_\alpha)}\mathcal{P}\middle|\mathbf{x}_{\alpha+1} + \frac{\Delta\mathbf{x}_{\alpha+1}}{2}\right\rangle e^{i\mathbf{p}_\alpha^T\Delta\mathbf{x}_\alpha}.$$
$$(25)$$

Using a high temperature approximation, define an $\mathcal{M}(\mathbf{R})$ matrix with elements given by

$$\mathcal{M}_{nm} = \langle n|e^{-\beta_N\mathcal{V}(\mathbf{R})}|m\rangle \qquad (26)$$

where

$$\mathcal{M}_{nm} = \begin{cases} e^{-\beta_N V_{nm}(\mathbf{R})} & n = m \\ -\beta_N V_{nm}(\mathbf{R})e^{-\beta_N V_{nm}(\mathbf{R})} & n \neq m \end{cases}. \qquad (27)$$

By making use of this notation and equation (13), equation (25) is written

$$I_E \propto \int d\{\mathbf{x}_\alpha\} \int d\{\mathbf{p}_\alpha\} \int d\{\Delta\mathbf{x}_\alpha\}$$

$$\prod_{\alpha=1}^{N} \left(\mathbf{x}_\alpha - \frac{\Delta\mathbf{x}_\alpha}{2}\right)^T \mathcal{M}(\mathbf{R}_\alpha) \left(\mathbf{x}_{\alpha+1} + \frac{\Delta\mathbf{x}_{\alpha+1}}{2}\right)$$

$$\exp\left[\sum_{\alpha=1}^{N} i\mathbf{p}_\alpha^T\Delta\mathbf{x}_\alpha - \frac{1}{2}\left(\mathbf{x}_\alpha + \frac{\Delta\mathbf{x}_\alpha}{2}\right)^2 \right.$$

$$\left. - \frac{1}{2}\left(\mathbf{x}_{\alpha+1} - \frac{\Delta\mathbf{x}_{\alpha+1}}{2}\right)^2\right]. \qquad (28)$$

Simplifying the exponent yeilds

$$i\mathbf{p}_\alpha^T\Delta\mathbf{x}_\alpha - \mathbf{x}_\alpha^2 - \frac{1}{4}\Delta\mathbf{x}_\alpha^2, \qquad (29)$$

and completing the square gives

$$-\frac{1}{4}\left((\Delta\mathbf{r}_\alpha - 2i\mathbf{p}_\alpha)^2 + 4\mathbf{x}_\alpha^2 + 4\mathbf{p}_\alpha^2\right). \qquad (30)$$

Substituting the exponent back into equation (28) and using the fact that for a product of matrices $ABCD = \mathrm{Tr}[D \otimes ABC]$,

$$I_E \propto \int d\{\mathbf{x}_\alpha\} \int d\{\mathbf{p}_\alpha\} \int d\{\Delta\mathbf{r}_\alpha\}$$

$$\mathrm{Tr}\left[\prod_{\alpha=1}^{N} \left(\mathbf{r}_\alpha - \frac{\Delta\mathbf{r}_\alpha}{2}\right) \otimes \left(\mathbf{r}_\alpha + \frac{\Delta\mathbf{r}_\alpha}{2}\right)^T \mathcal{M}(\mathbf{R}_\alpha)\right]$$

$$\exp\left[-\frac{1}{4}\sum_{\alpha=1}^{N}(\Delta\mathbf{x}_\alpha - 2i\mathbf{p}_\alpha)^2 + 4\mathbf{x}_\alpha^2 + 4\mathbf{p}_\alpha^2\right]. \qquad (31)$$

Now with the substitution $\mathbf{u}_\alpha = \Delta\mathbf{r}_\alpha - 2i\mathbf{p}_\alpha$,

$$I_E \propto \int d\{\mathbf{x}_\alpha\} \int d\{\mathbf{p}_\alpha\} \exp\left[-\sum_{\alpha=1}^{N} \mathbf{x}_\alpha^2 + \mathbf{p}_\alpha^2\right]$$

$$\int d\{\mathbf{u}_\alpha\} \operatorname{Tr}\left[\prod_{\alpha=1}^{N}\left(\mathbf{x}_\alpha + i\mathbf{p}_\alpha + \frac{\mathbf{u}_\alpha}{2}\right)\right.$$

$$\left.\otimes\left(\mathbf{x}_\alpha - i\mathbf{p}_\alpha - \frac{\mathbf{u}_\alpha}{2}\right)^T \mathcal{M}(\mathbf{R}_\alpha)\right] \exp\left[-\frac{1}{4}\sum_{\alpha=1}^{N} \mathbf{u}_\alpha^2\right]. \quad (32)$$

By expanding equation (32),

$$I_E \propto \int d\{\mathbf{x}_\alpha\} \int d\{\mathbf{p}_\alpha\} \exp\left[-\sum_{\alpha=1}^{N} \mathbf{x}_\alpha^2 + \mathbf{p}_\alpha^2\right]$$

$$\int d\{\mathbf{u}_\alpha\} \operatorname{Tr}\left[\prod_{\alpha=1}^{N}(\mathbf{x}_\alpha + i\mathbf{p}_\alpha) \otimes (\mathbf{x}_\alpha - i\mathbf{p}_\alpha)^T\right.$$

$$-\frac{1}{2}(\mathbf{x}_\alpha + i\mathbf{p}_\alpha)\otimes\mathbf{u}_\alpha^T + \frac{1}{2}\mathbf{u}_\alpha \otimes (\mathbf{x}_\alpha + i\mathbf{p}_\alpha)^T$$

$$\left.-\frac{1}{4}\mathbf{u}_\alpha\otimes\mathbf{u}_\alpha^T\mathcal{M}(\mathbf{R}_\alpha)\right] \exp\left[-\frac{1}{4}\sum_{\alpha=1}^{N} \mathbf{u}_\alpha^2\right], \quad (33)$$

the integral in $\mathbf{u}_\alpha$ can be evaluated by comparison with the Gaussian integrals $\int_{-\infty}^{\infty} e^{-ax^2} dx = \left(\frac{\pi}{a}\right)^{1/2}$, $\int_{-\infty}^{\infty} xe^{-ax^2} dx = 0$, and $\int_{-\infty}^{\infty} x^2 e^{-ax^2} dx = \frac{1}{2}\left(\frac{\pi}{a^3}\right)^{1/2}$. This gives

$$I_E \propto \int d\{\mathbf{x}_\alpha\} \int d\{\mathbf{p}_\alpha\} \exp\left[-\sum_{\alpha=1}^{N} \mathbf{x}_\alpha^2 + \mathbf{p}_\alpha^2\right]$$

$$\operatorname{Tr}\left[\prod_{\alpha=1}^{N}\left((\mathbf{x}_\alpha + i\mathbf{p}_\alpha)\otimes(\mathbf{x}_\alpha - i\mathbf{p}_\alpha)^T - \frac{1}{2}\mathcal{I}\right)\mathcal{M}(\mathbf{R}_\alpha)\right]. \quad (34)$$

Now inserting I_E back into equation (7), we have

$$Z \propto \lim_{N\to\infty} \int d\{\mathbf{R}_\alpha\} \int d\{\mathbf{P}_\alpha\} \int d\{\mathbf{r}_\alpha\} \int d\{\mathbf{p}_\alpha\}\, e^{-\beta_N H_{MV}} \quad (35)$$

where

$$H_{MV} = \sum_{\alpha=1}^{N}\left[\frac{\mathbf{P}_\alpha^2}{2M} + V_0(\mathbf{R}_\alpha) + \frac{M}{2\beta_N^2}(\mathbf{R}_\alpha - \mathbf{R}_{\alpha+1})^2\right.$$

$$\left.+ \frac{1}{\beta_N}\left(\mathbf{x}_\alpha^2 + \mathbf{p}_\alpha^2\right)\right] - \frac{1}{\beta_N}\ln\left|\operatorname{Re}[\operatorname{Tr}[\boldsymbol{\Gamma}]]\right|, \quad (36)$$

and

$$\boldsymbol{\Gamma} = \prod_{\alpha=1}^{N}\left((\mathbf{x}_\alpha + i\mathbf{p}_\alpha)\otimes(\mathbf{x}_\alpha - i\mathbf{p}_\alpha)^T - \frac{1}{2}\mathcal{I}\right)\mathcal{M}(\mathbf{R}_\alpha). \quad (37)$$

2.4 Coherent State Ring Polymer

The CS-RPMD derivation begins by writing I_E as a trace over $\mathbf{x}$ by removing the identities from equation (9)

$$I_E = \int d\mathbf{x}_1 \langle\mathbf{x}_1| \prod_{\alpha=1}^{N} e^{-\beta_N \mathcal{V}(\mathbf{R}_\alpha)}|\mathbf{x}_1\rangle \quad (38)$$

$$= \operatorname{Tr}\left[\prod_{\alpha=1}^{N} e^{-\beta_N \mathcal{V}(\mathbf{R}_\alpha)}\right]. \quad (39)$$

Using the Taylor expansion $e^x = \sum_{n=0}^{\infty} x^n/n!$,

$$I_E = \operatorname{Tr}\prod_{\alpha=1}^{N}\left[1 - \beta_N \sum_{n,m} V_{nm}(\mathbf{R}_\alpha)\hat{a}_n^\dagger \hat{a}_m + \mathcal{O}(\beta_N^2)\right], \quad (40)$$

and the commutation relation $[\hat{a}_m, \hat{a}_n^\dagger] = \delta_{mn}$,

$$I_E \approx \operatorname{Tr}\prod_{\alpha=1}^{N}\left[1 - \beta_N \sum_{n,m} V_{nm}(\mathbf{R}_\alpha)(\hat{a}_m\hat{a}_n^\dagger - \delta_{mn})\right]. \quad (41)$$

Inserting the identity over coherent states,

$$\hat{I} = \left(\frac{1}{2\pi}\right)^L \int d\mathbf{p}\,d\mathbf{q}\,|\mathbf{p}, \mathbf{q}\rangle\langle\mathbf{p}, \mathbf{q}|, \quad (42)$$

N times gives

$$I_E \propto \int d\{\mathbf{p}_\alpha\} \int d\{\mathbf{q}_\alpha\} \operatorname{Tr}\prod_{\alpha=1}^{N}\left[|\mathbf{p}_\alpha, \mathbf{q}_\alpha\rangle\langle\mathbf{p}_\alpha, \mathbf{q}_\alpha|\right.$$

$$- \beta_N \sum_{n,m} V_{nm}(\mathbf{R}_\alpha)(\hat{a}_m|\mathbf{p}_\alpha, \mathbf{q}_\alpha\rangle\langle\mathbf{p}_\alpha, \mathbf{q}_\alpha|\hat{a}_n^\dagger -$$

$$\left.\delta_{mn}|\mathbf{p}_\alpha, \mathbf{q}_\alpha\rangle\langle\mathbf{p}_\alpha, \mathbf{q}_\alpha|)\right] \quad (43)$$

and since coherent states are eigenstates of $\hat{a}^\dagger$ and $\hat{a}$,

$$I_E \propto \int d\{\mathbf{p}_\alpha\} \int d\{\mathbf{q}_\alpha\}$$

$$\operatorname{Tr}\prod_{\alpha=1}^{N}\left[|\mathbf{p}_\alpha, \mathbf{q}_\alpha\rangle\langle\mathbf{p}_\alpha, \mathbf{q}_\alpha|\left(1 - \beta_N \sum_{n,m} V_{nm}(\mathbf{R}_\alpha)\right.\right.$$

$$\left.\left.\left(\frac{1}{2}[\mathbf{q}_\alpha + i\mathbf{p}_\alpha]_m[\mathbf{q}_\alpha - i\mathbf{p}_\alpha]_n - \delta_{mn}\right)\right)\right]. \quad (44)$$

Using the fact that for a product of matrices $ABCD = \operatorname{Tr}[D\otimes ABC]$, and inserting the diabatic projection operator $\mathcal{P} = \sum_n |n\rangle\langle n|$,

$$I_E \propto \int d\{\mathbf{p}_\alpha\} \int d\{\mathbf{q}_\alpha\}$$

$$\prod_{\alpha=1}^{N}\left[\sum_n \langle\mathbf{p}_\alpha, \mathbf{q}_\alpha|n\rangle\langle n|\mathbf{p}_{\alpha+1}, \mathbf{q}_{\alpha+1}\rangle\left(1 - \beta_N \sum_{n,m} V_{nm}(\mathbf{R}_\alpha)\right.\right.$$

$$\left.\left.\left(\frac{1}{2}[\mathbf{q}_\alpha + i\mathbf{p}_\alpha]_m[\mathbf{q}_\alpha - i\mathbf{p}_\alpha]_n - \delta_{mn}\right)\right)\right]. \quad (45)$$

By equations (14) and (15),

$$I_E \propto \int d\{\mathbf{p}_\alpha\} \int d\{\mathbf{q}_\alpha\}$$

$$\prod_{\alpha=1}^{N} \left[(\mathbf{q}_\alpha - i\mathbf{p}_\alpha)^T (\mathbf{q}_{\alpha+1} + i\mathbf{p}_{\alpha+1}) \right]$$

$$\exp\left[\sum_{\alpha=1}^{N} -\frac{1}{4}\left(\mathbf{q}_\alpha^2 + \mathbf{p}_\alpha^2 + \mathbf{q}_{\alpha+1}^2 + \mathbf{p}_{\alpha+1}^2 \right) - \beta_N \sum_{n,m} V_{nm}(\mathbf{R}_\alpha) \right.$$

$$\left. \left(\frac{1}{2}([\mathbf{q}_\alpha]_m[\mathbf{q}_\alpha]_n + [\mathbf{p}_\alpha]_m[\mathbf{p}_\alpha]_n) - \delta_{mn} \right) \right], \quad (46)$$

which can be rewritten as

$$I_E \propto \int d\{\mathbf{p}_\alpha\} \int d\{\mathbf{q}_\alpha\}$$

$$\mathrm{Tr}\left[\prod_{\alpha=1}^{N} \left[(\mathbf{q}_\alpha + i\mathbf{p}_\alpha) \otimes (\mathbf{q}_\alpha - i\mathbf{p}_\alpha)^T \right] \right]$$

$$\exp\left[\sum_{\alpha=1}^{N} -\frac{1}{2}\left(\mathbf{q}_\alpha^2 + \mathbf{p}_\alpha^2 \right) - \right.$$

$$\left. \beta_N \,\mathrm{Tr}\left[\mathcal{V}(\mathbf{R}_\alpha) \left(\frac{1}{2\hbar}(\mathbf{q}_\alpha \otimes \mathbf{q}_\alpha^T + \mathbf{p}_\alpha \otimes \mathbf{p}_\alpha^T) - \mathcal{I} \right) \right] \right]. \quad (47)$$

Now inserting I_E back into equation (7), we have

$$Z \propto \lim_{N \to \infty} \int d\{\mathbf{R}_\alpha\} \int d\{\mathbf{P}_\alpha\} \int d\{\mathbf{p}_\alpha\} \int d\{\mathbf{q}_\alpha\}\, e^{-\beta_N H_{CS}} \quad (48)$$

where

$$H_{CS} = \sum_{\alpha=1}^{N} \left[\frac{\mathbf{P}_\alpha^2}{2M} + V_0(\mathbf{R}_\alpha) + \frac{M}{2\beta_N^2}(\mathbf{R}_\alpha - \mathbf{R}_{\alpha+1})^2 \right.$$

$$+ \frac{1}{2\beta_N}\left(\mathbf{q}_\alpha^2 + \mathbf{p}_\alpha^2 \right)$$

$$\left. + \mathrm{Tr}\left[\mathcal{V}(\mathbf{R}_\alpha) \left(\frac{1}{2}(\mathbf{q}_\alpha \otimes \mathbf{q}_\alpha^T + \mathbf{p}_\alpha \otimes \mathbf{p}_\alpha^T) - \mathcal{I} \right) \right] \right]$$

$$- \frac{1}{\beta_N} \ln \left| \mathrm{Re}[\mathrm{Tr}[\boldsymbol{\Gamma}]] \right|, \quad (49)$$

and

$$\boldsymbol{\Gamma} = \prod_{\alpha=1}^{N} (\mathbf{q}_\alpha + i\mathbf{p}_\alpha) \otimes (\mathbf{q}_\alpha - i\mathbf{p}_\alpha)^T. \quad (50)$$

2.5 Alternate Coherent State Form

A different derivation involving coherent states involves performing the trace in equation (39) over coherent states, so that

$$I_E = \int d\mathbf{p} \int d\mathbf{q} \langle \mathbf{p}, \mathbf{q}| \prod_{\alpha=1}^{N} e^{-\beta_N \mathcal{V}(\mathbf{R}_\alpha)} |\mathbf{p}, \mathbf{q}\rangle. \quad (51)$$

Then by inserting $N-1$ coherent state identities, similarly to the path integral procedure, we obtain

$$I_E = \int d\{\mathbf{p}_\alpha\} \int d\{\mathbf{q}_\alpha\}$$

$$\prod_{\alpha=1}^{N} \langle \mathbf{p}_\alpha, \mathbf{q}_\alpha| e^{-\beta_N \mathcal{V}(\mathbf{R}_\alpha)} |\mathbf{p}_{\alpha+1}, \mathbf{q}_{\alpha+1}\rangle. \quad (52)$$

By expanding the exponential,

$$I_E \approx \int d\{\mathbf{p}_\alpha\} \int d\{\mathbf{q}_\alpha\} \prod_{\alpha=1}^{N} \langle \mathbf{p}_\alpha, \mathbf{q}_\alpha|$$

$$\left[1 - \beta_N \sum_{n,m} V_{nm}(\mathbf{R}_\alpha)\hat{a}_m^\dagger \hat{a}_n \right] |\mathbf{p}_{\alpha+1}, \mathbf{q}_{\alpha+1}\rangle, \quad (53)$$

and by distributing the states through each term and inserting $\mathcal{P}$, I_E becomes

$$I_E \approx \int d\{\mathbf{p}_\alpha\} \int d\{\mathbf{q}_\alpha\} \prod_{\alpha=1}^{N} \langle \mathbf{p}_\alpha, \mathbf{q}_\alpha|\mathcal{P}|\mathbf{p}_{\alpha+1}, \mathbf{q}_{\alpha+1}\rangle$$

$$\left[1 - \beta_N \sum_{n,m} V_{nm}(\mathbf{R}_\alpha)[\mathbf{q}_\alpha - i\mathbf{p}_\alpha]_m[\mathbf{q}_{\alpha+1} + i\mathbf{p}_{\alpha+1}]_n \right]. \quad (54)$$

Carrying out the derivation as before, we find

$$H_{CS} = \sum_{\alpha=1}^{N} \left[\frac{\mathbf{P}_\alpha^2}{2M} + V_0(\mathbf{R}_\alpha) + \frac{M}{2\beta_N^2}(\mathbf{R}_\alpha - \mathbf{R}_{\alpha+1})^2 \right.$$

$$+ \frac{1}{2\beta_N}\left(\mathbf{q}_\alpha^2 + \mathbf{p}_\alpha^2 \right)$$

$$\left. + \frac{1}{2}\mathrm{Tr}\left[\mathcal{V}(\mathbf{R}_\alpha)(\mathbf{q}_\alpha \otimes \mathbf{q}_{\alpha+1}^T + \mathbf{p}_\alpha \otimes \mathbf{p}_{\alpha+1}^T) \right] \right]$$

$$- \frac{1}{\beta_N} \ln \left| \mathrm{Re}[\mathrm{Tr}[\boldsymbol{\Gamma}]] \right|, \quad (55)$$

and

$$\boldsymbol{\Gamma} = \prod_{\alpha=1}^{N} (\mathbf{q}_\alpha + i\mathbf{p}_\alpha) \otimes (\mathbf{q}_\alpha - i\mathbf{p}_\alpha)^T. \quad (56)$$

2.6 Multi-State Instantons

The instanton configuration is the first-order saddle point of the effective potential. [7] This is well established and is predicted to be true for multiple electronic states as well.

3 Implementation Details

The same procedures were used for both the Mapping Variable and Coherent State cases. Although for

the mapping variable case, a version of the Hamiltonian was used which did not include the electronic momentum,

$$H = \sum_{\alpha=1}^{N} \left[\frac{\mathbf{P}_\alpha^2}{2M} + V_0(\mathbf{R}_\alpha) + \frac{M}{2\beta_N^2}(\mathbf{R}_\alpha - \mathbf{R}_{\alpha+1})^2 \right.$$
$$\left. + \frac{1}{\beta_N}\mathbf{x}_\alpha^2 \right] - \frac{1}{\beta_N} \ln|\mathbf{\Gamma}| \quad (57)$$

where

$$\mathbf{\Gamma} = \prod_{\alpha=1}^{N} \mathbf{x}_\alpha^T \mathcal{M}(\mathbf{R}_\alpha)\mathbf{x}_{\alpha+1}. \quad (58)$$

In each case, the effective potential was taken to be the Hamiltonian, neglecting the nuclear kinetic energy term and the electronic-state independent potential (V_0). The potential, its gradient, and its hessian were written in Python. The potential was minimized using the l-bfgs-b algorithm from scipy.optimize, [6] using an approximate gradient. The resulting values for $\mathbf{R}_\alpha$ and $\mathbf{x}_\alpha$ (and $\mathbf{p}_\alpha$ for the Coherent State case) were then used to compute the hessian of the effective potential. The eigenvalues and eigenvectors were computed by numpy.linalg.eigh.

The electronic state populations for each bead were found from the electronic position and momentum variables, using a Wigner Estimator. For the Mapping Variable formulation, the populations were calculated from

$$[\mathbf{x}_\alpha]_n^2, \quad (59)$$

since it was not written to include electronic momentum variables. For the Coherent State formulation, the populations were found using

$$\frac{[\mathbf{x}_\alpha]_m^2 + [\mathbf{p}_\alpha]_m^2}{\sum_n [\mathbf{x}_\alpha]_n^2 + [\mathbf{p}_\alpha]_n^2}. \quad (60)$$

Our model used the two state potential

$$\mathcal{V} = \begin{bmatrix} \frac{1}{2}M\omega^2(r+5)^2 & \Delta \\ \Delta & \frac{1}{2}M\omega^2(r-5)^2 \end{bmatrix}. \quad (61)$$

Where $M = 2$ and $\omega = 1$. The non-adiabatic limit corresponds to when $\Delta \to 0$, we found the instanton for the adiabatic case (high coupling, $\Delta = 0.8$) and for the non-adiabatic case (low coupling, $\Delta = 0.01$. We also varied the reciprocal temperature between $\beta = 2.5$ and $\beta = 5.0$. Our initial guesses for the optimization were

$$R_\alpha = \cos(2\pi\alpha/N), \quad (62)$$

$$[\mathbf{x}_\alpha]_1 = [\mathbf{p}_\alpha]_1 = \sqrt{\frac{e^{-\beta_N V_{11}}}{e^{-\beta_N V_{11}} + e^{-\beta_N V_{22}}}}, \quad (63)$$

and

$$[\mathbf{x}_\alpha]_2 = [\mathbf{p}_\alpha]_2 = \sqrt{\frac{e^{-\beta_N V_{22}}}{e^{-\beta_N V_{11}} + e^{-\beta_N V_{22}}}}. \quad (64)$$

4   Results and Discussion

The path integral representation is exact in the limit of $N \to \infty$, so as we increase the number of beads, we expect the instanton to converge to a single configuration. This is observed early on in the mapping variable case, as figure 3 shows convergence for $\beta = 2.5$ at $N = 128$. The coherent state case however, for the same parameters, has still not converged by $N = 512$, as shown in figure 4.
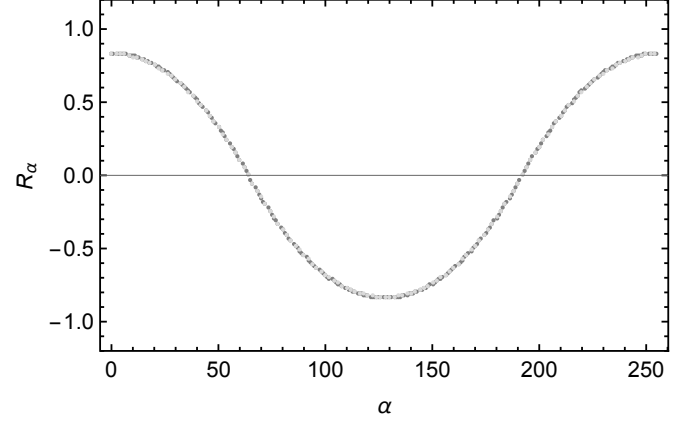

Figure 3: Nuclear bead positions for the H_{MV} potential with $\beta = 2.5$ and $\Delta = 0.8$ for $N = 128$ (light gray) and $N = 256$ (gray)
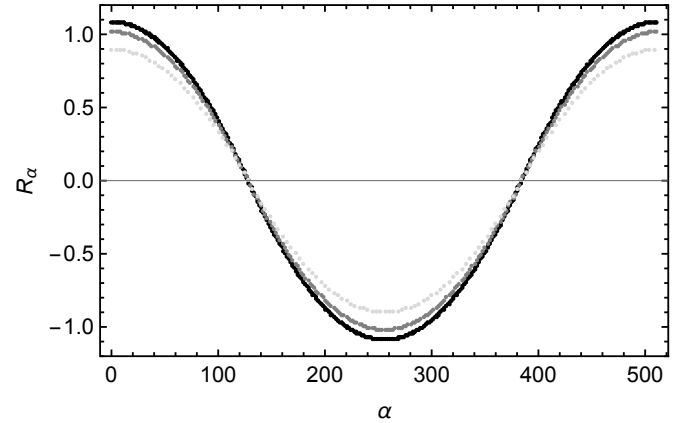

Figure 4: Nuclear bead positions for the H_{CS} potential with $\beta = 2.5$ and $\Delta = 0.8$ for $N = 128$ (light gray), $N = 256$ (gray), and $N = 512$ (black)

For the coherent state case with $\beta = 5.0$, convergence occurred quickly figure 5 shows that the instanton has converged by $N = 128$. The bead positions for this case flatten out when they reach -5 and 5, accumulating in the bottom of the potential wells given in equation (55). It was observed that all CS instantons which stretched to the bottom of the wells (those with $\beta > 5.0$) converged. This suggests that the minimizing algorithm is finding this position to be a strong minimum. If the frequency of the initial guess is doubled (so that the ring polymer

34

is draped over the barrier twice, with an initial guess of $R_\alpha = \cos(4\pi\alpha/N))$, then the coherent state $\beta = 5$ case no longer converges, and its amplitude begins growing as the number of beads increases. With two cycles, $\beta = 5.0$ is now behaving more like $\beta = 2.5$, as can be seen in figure 6. This is expected because below certain temperatures (above some $\lambda\beta_c$), the instanton folds back on itself λ times. [7]
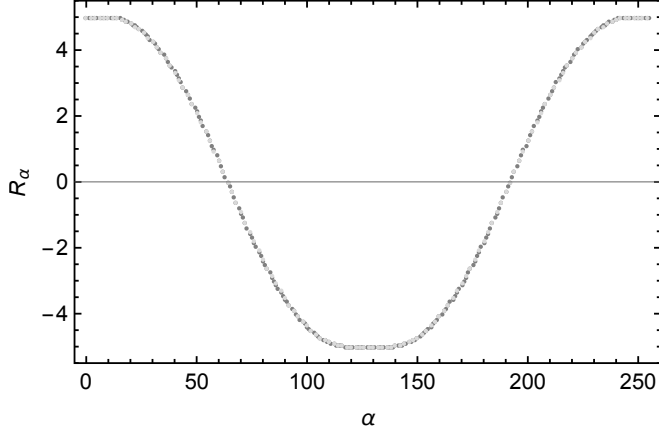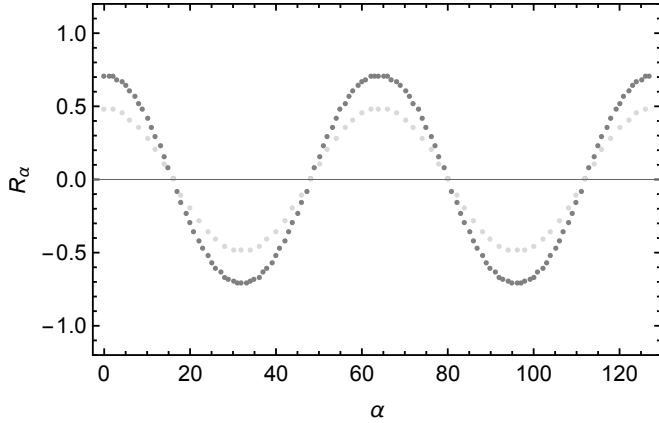

Figure 5: Nuclear bead positions for the H_{CS} potential with $\beta = 5.0$ and $\Delta = 0.8$ for $N = 128$ (light gray) and $N = 256$ (gray)

Figure 6: Nuclear bead positions for the H_{CS} potential with an initial guess of $R_\alpha = \cos(4\pi\alpha/N)$, $\beta = 5.0$ and $\Delta = 0.8$ for $N = 64$ (light gray) and $N = 128$ (gray)

The CS instantons are also consistently greater than the MV results, at a high enough bead count, as is illustrated in figure 7 and 8. And by comparing the scales on those two figures, it is confirmed for both CS and MV instantons that the amplitude decreases with increasing temperature (decreasing β). The results for the alternate CS Instanton however, with $\beta = 2.5$ and $\Delta = 0.8$, given in figure 9 were less than the corresponding MV instanton by $N = 256$. Though at that point, like the original CS Instanton, it has yet to converge. So it is possible that when it does converge, it will be close to the MV instanton.
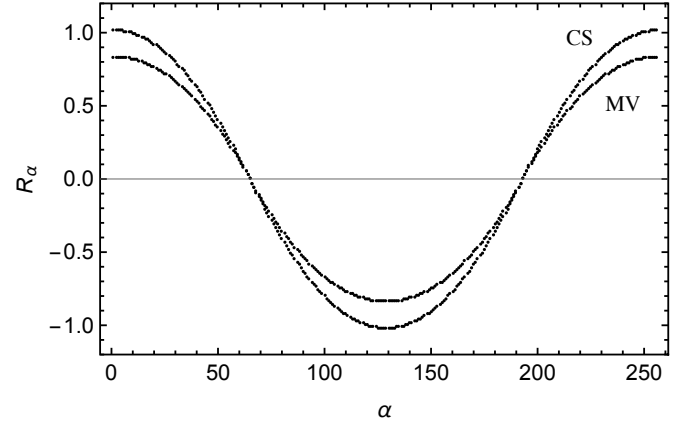

Figure 7: Nuclear bead positions for both the H_{CS} potential and the H_{MV} potential, with $\beta = 2.5$ and $\Delta = 0.8$ for $N = 256$
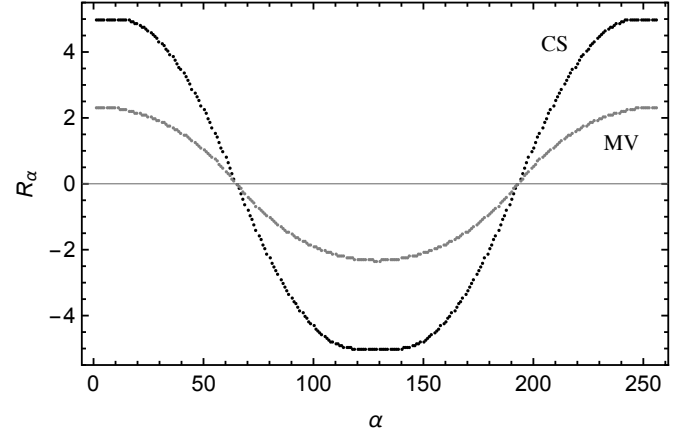

Figure 8: Nuclear bead positions for both the H_{CS} potential and the H_{MV} potential, with $\beta = 5.0$ and $\Delta = 0.8$ for $N = 256$

The populations for the two cases are much more similar than the bead positions are. It is shown in figure 10 the beads closest to a given state have a population of approximately 1 for that state and 0 for the other. The beads in the middle each have a population of about 0.5, so it experiences an equal influence from both states. Some of the populations wrinkle up a bit before switching between 0 and 1. These parts of the curves are shown in 11. The transition appears to become smoother in both the mapping variable and coherent state populations for lower temperatures (increasing β) and lower coupling between states (decreasing Δ).

5 Conclusions and Future Work

The nuclear ring polymer Hamiltonian was derived and used as a starting spot for deriving the mapping vari-
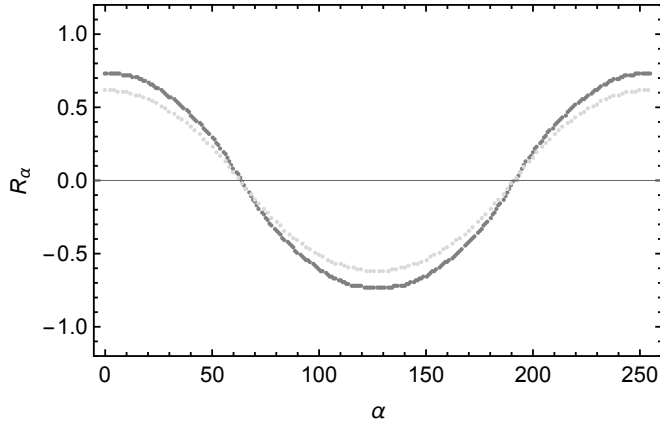
Figure 9: Nuclear bead positions the alternate H_{CS} potential, with $\beta = 2.5$ and $\Delta = 0.8$ for $N = 128$ (light gray) and $N = 256$ (gray)
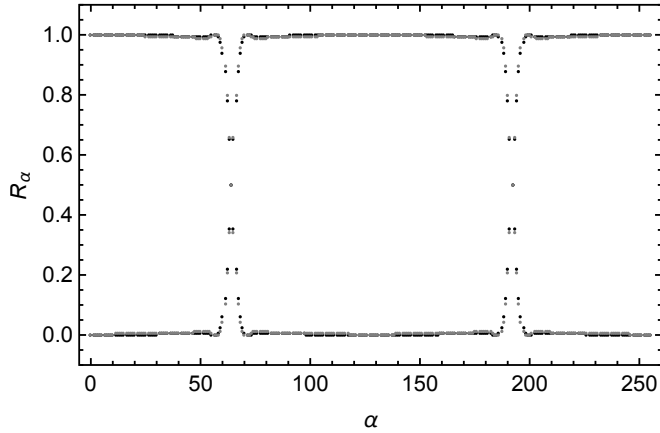

Figure 10: Populations for $N = 256$, black denotes coherent state and gray denotes mapping variable

able and coherent state Hamiltonians, by way of Stock-Thoss mapping from discrete electronic states to continuous bases. An alternate form of the coherent state Hamiltonian was also proposed. The bead positions did not converge for a reasonable number of beads in the coherent state case, and appeared to be moving away from those in the mapping variable case. There were other challenges which were not discussed, such as how the MV hessian would consistently yield one negative eigenvalue and $N - 1$ positive eigenvalues (indicating a first order saddle point), while the CS hessian would consistently give one negative eigenvalue and $N - 1$ approximately 0 eigenvalues. This and the differences in the nuclear instantons, despite the similar derivations and exact nature, warrant further study.

Acknowledgements

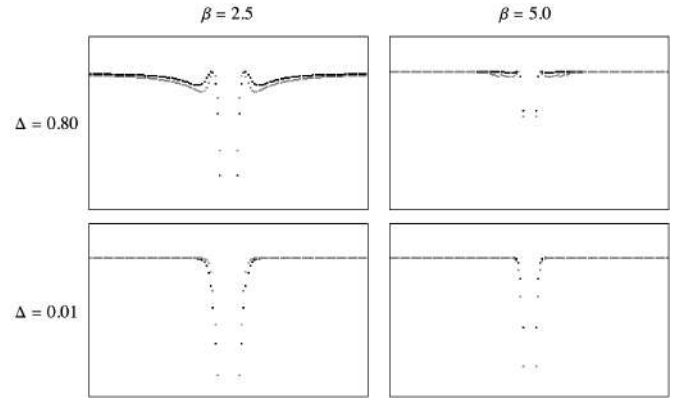I would like to thank Dr. Nandini Ananth, for her support this summer, and for inventing MV-RPMD. I would

Figure 11: Zoomed in populations for $N = 256$, black denotes coherent state and gray denotes mapping variable, each plot is from beads 128 to 256 on the horizontal axis and from population 0.92 to 1.02 on the vertical axis

References

[1] J. Richardson et. al., *Science* **351** (6279), 1310-1313.

[2] M. Tuckerman, *Statistical Mechanics: Theory and Simulation*, Oxford University Press: New York, 2010.

[3] N. Ananth, J. Chem. Phys. **139**, 124102 (2013).

[4] S. Chowdhury and P. Huo, J. Chem. Phys. **147**, 124109 (2017).

[5] G. Stock and M. Thoss, Phys. Rev. Lett. **78**, 578 (1997).

[6] R. H. Byrd, P. Lu and J. Nocedal. A Limited Memory Algorithm for Bound Constrained Optimization, (1995), SIAM Journal on Scientific and Statistical Computing, 16, 5, pp. 1190-1208.

[7] J. Richardson and S. Althorpe, J. Chem. Phys. **131**, 214106 (2009).

The Statistics of the A-B Transition of ^{3}He in Thin Slab Confinement

John Wilson[1,2], Dmytro Lotnyk [2], Michael Terilli[2], and Jeevak Parpia[2]

[1]State University of New York at Geneseo, Geneseo, New York [2]Cornell
Center for Materials Research, Cornell University, Ithaca, New York

Helium 3 has two superfluid phases. The transition between these phases is first order, display-ing hysteresis and supercooling. Here, the effects of confinement to a thin slab geometry on this phase transition are presented. A 1.1 μm channel connected two chambers filled with liquid helium 3. The first chamber, the heat exchange chamber, was heated and cooled via adiabatic nuclear magnetization. Quartz tuning forks being driven by an AC current were present in both chambers. The frequency and Q factor of these forks were directly measured. Phase transitions correspond to discontinuities within both the Q factor and the frequency of these forks, allowing for the state of the fluid to be inferred. Using this, the location of the A to B transition in the bulk regions were mapped.

I. INTRODUCTION

Helium is the second most common element in the universe. In nature it has two common isotopes: ^{3}He and ^{4}He. ^{3}He is a fermion with a nuclear spin of $\frac{1}{2}$. As a result, ^{3}He obeys Fermi-Dirac statistics and, by proxy, the Pauli Exclusion Principle. ^{4}He however, is a boson with a spin of 0. ^{4}He therefore obeys Bose-Einstein statistics, and notably does not obey the Pauli Exclusion Principle. Both isotopes exhibit interesting properties in low temperature ranges. At atmospheric pressure, helium is the only element to stay liquid until temperatures near absolute zero [4]. Furthermore, both types of isotopes undergo superfluid transitions at low temperatures. A superfluid is a purely quantum mechanical system. As a result, they each provide systems that are extremely interesting to physicists.

II. MOTIVATION

^{4}He undergoes a superfluid transition at 2.17 K at vapor pressure. ^{3}He meanwhile, undergoes its superfluid transition at a much lower temperature of about 1 mK at vapor pressure. Their superfluid transitions differ in temperature by orders of magnitude due to the different statistics governing their composite atoms. This extreme nature of superfluid ^{3}He causes it to be harder to study in its superfluid state, but also much more complex and interesting.

A. Theory

^{3}He was theorized to have many different phases of superfluidity. Two sets of scientists each posited the existence of one of the two phases that actually were observed in the bulk. Anderson and Morel proposed a phase with non-s-wave [5] pairing states with two spin substates of $S_z = \pm1$. This became identified with the A Phase. Balian and Werthamer proposed a p-state that could con-

tain the $S_z = \pm1$ spin substates as well as the $S_z = 0$ spin substate [1]. This was identified to be the B phase. The first observation of superfluid ^{3}He in 1971 was the subject of the 1996 Nobel Prize, awarded to Lee, Richardson and Osheroff at Cornell.

The existence of two superfluid phases with different possible spin substates creates a system that is much more complex than that of superfluid ^{4}He. Furthermore, the transition between these two phases is first order and provides a chance to learn a lot about phase transitions in a system that is purely quantum mechanical [1]. The phases of ^{3}He can be seen in Figure 1.
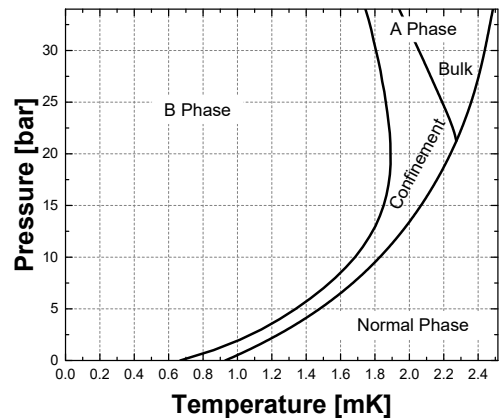

FIG. 1. The Phase Diagram of ^{3}He. Note the poly critical point at a Pressure of 21.22 bar and Temperature of 2.23 mK. The poly critical point is where the A phase and B phase have the same free energy at the superfluid transition. It is also the meeting point of the first order (A to B) transition and second order (Tc vs P) lines. The region close to this poly critical point is of great interest.

^{3}He's net magnetic dipole leads to interesting interactions to study. This net dipole leads to interactions with magnetic fields. This net magnetic dipole also causes superfluid ^{3}He to resemble metallic superconductors. When

^{3}He undergoes its superfluid transition, the individual atoms act similarly to electrons in Cooper pairs. In the formation of Cooper pairs, an electron travels through a lattice of heavy, positively charged particles. As it travels, a small positive "wake" forms behind it. At low enough temperatures, this positively charged wake is not re-equilibrated. Another electron traveling will be attracted to that positively charged wake, and thus effectively to the first electron [1].

In liquid ^{3}He this interaction does not happen at lattice sites, but instead within the viscous liquid. A traveling ^{3}He particle will leave a wake of spin polarization opposite to its own. At low enough temperatures, this wake remains long enough for a second ^{3}He particle to interact with that wake. The second ^{3}He will see the wake as an oppositely polarized magnetic dipole, and be attracted to it. As a result, the ^{3}He atoms will essentially be attracted to each other and align their magnetic dipoles to be parallel with each other. The result is two ^{3}He particles that now form a ^{3}He cooper pair with a spin of 1. This integer spin means the pair can now be described with Bose-Einstein statistics, and form a superfluid [1].

B. Effects of Confinement

In this paper, we will describe the observation of these transition points in the bulk fluid cooled through a thin slab. Confining the ^{3}He to a thin slab geometry changes the interparticle interactions by reducing the dimensions of the chamber to below the the mean free path of thermal transport in the bulk. This allows the A phase to form at pressures and temperatures lower than it otherwise would in the bulk phase, as seen in Figure 1, because confinement energetically favors the A phase over the B phase. Within the channel, the A phase is promoted over the B phase because of the manner in which ^{3}He particles orbit each other as a cooper pair. Thus, the mechanism causing nucleation of the bulk B phase from the A phase may be studied more closely. Confinement also changes properties of heat flow within the system. This creates an interesting setting for the response and relaxation times of a perturbed system to be studied.

III. EXPERIMENTAL APPARATUS

In the field of low temperature physics, there are many difficulties to overcome. Reaching low temperatures, measuring the low temperatures without disturbing the system, isolating the experimental apparatus, and transferring cold liquid as well as heat are a few of these [2]. There are also a number of steps prior to cooling that involve purifying the helium gas. Due to how specific each of these steps are, they will not be discussed in detail here. These many challenges cause experimental apparatuses in low temperature physics to require multiple stages and methods for cooling.

A. Overview

The apparatus used to carry out this experiment is no exception. A brief overview of the setup is presented here and expanded on in later subsections. A precooling stage liquefies the helium before it is transferred to the main dewar. Liquid helium is transferred periodically [6] into the dewar. Inside this dewar, there is an insulated vacuum vessel immersed inside a tank filled with liquid ^{4}He. ^{4}He is continuously admitted into the chamber, called the 1 K pot. There it is pumped on to achieve a temperature of around 1.2 K. At the same time, pure ^{3}He is pumped on in the still of a dilution refrigerator and then returned into the refrigerator. The ^{3}He is precooled by the ^{4}He liquid, and then sent for further heat exchanging in the refrigerator. There a dilute mixture is used to cool the pure ^{3}He further in a series of heat step exchangers. See Figure 2.

Pure ^{3}He is independently admitted into the sample chambers. These chambers are linked to the nuclear cooling stage where adiabatic nuclear demagnetization occurs. In the nuclear demagnetization stage, metal nuclei are manipulated with a magnetic field to take advantage of their spin entropy and vary their temperature. This metal cools the heat exchange chamber. The heat exchange chamber is connected to the isolated chamber via a 1.1 μm height channel. The quartz tuning forks are located in these two chambers, and the experiment is carried out within these two. See Figure 3 for a diagram of these chambers.

B. The Precooling Stage

The precooling stage involves liquefying and pumping on ^{4}He. Pumping on a liquid bath decreases the pressure above the liquid. Inherent vapor pressure causes the most energetic of the atoms to leave the liquid at sufficiently low pressures. This process carries away some of the heat from the liquid bath. However, pumping on liquid ^{4}He below 1K more than 50% of the ^{4}He may be lost due to this process. Pumping much past this point serves only to offset a heat leak, albeit inefficiently.

C. Dilution Refrigerator

Prior to entering the dilution refrigerator, ^{3}He is precooled by contact with ^{4}He bath at 4 K. It is then liquefied by contact with the pumped ^{4}He bath at 1.2 K. This ^{3}He is sent into heat step exchangers. These heat step exchangers are cooled by a ^{3}He/^{4}He dilution refrigerator. This is depicted in Figure 2. The fridge operates by taking advantage of Fermi-Dirac statistics of the ^{3}He. A small amount of ^{3}He, 6.4% exactly at 0 K, may be dissolved into solution in superfluid ^{4}He at vapor pressure. In this solution it makes sense to approximate the ^{3}He particles as having a slightly heavier mass. This is

because of the Kelvin drag [7]. In the mixing chamber of the dilution refrigerator liquid ^{3}He sits in its normal state on top of the dilute mixture.
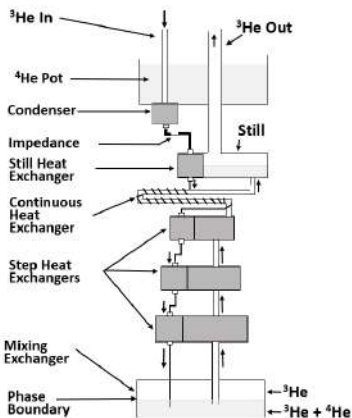

FIG. 2. A labeled diagram of the dilution refrigerator. Note the still where the dilute mix is pumped on is separate from the mixing chamber. Diagram based off a similar diagram from Experimental Principles and Methods Below 1K [2].

This dilute mixture of ^{3}He in solution in superfluid ^{4}He is pumped on in a still above the mixing chamber. ^{3}He atoms are removed first because of their higher vapor pressure. As ^{3}He is removed, the remaining solution is cooled via evaporative effects. The ^{3}He gas is removed and recirculated back into the fridge. A ^{4}He liquid pot cools the incoming ^{3}He to about 1.1K. The pressure is kept high on the ^{3}He so it condenses back into liquid form. The ^{3}He is then cooled by the dilute mixture as it is added back into the mixing chamber through step heat exchangers. When ^{3}He is put back into the mixing chamber, the atoms will find it energetically favorable not to enter the dilute mixture again. As a result, as the ^{3}He atoms are returned, they return to the pure ^{3}He side. When the hotter atoms of ^{3}He from the still are drawn off, this results in the extraction of ^{3}He from the dilute side of the mixture. To maintain the concentration of ^{3}He in ^{4}He at 6.4%, enough ^{3}He atoms will cross the ^{3}He to ^{3}He - ^{4}He interface to maintain a constant distribution of momenta in the pure and dilute solutions. The act of crossing from the pure to dilute mix is similar to evaporation. As a result, it lowers the energy of the dilute mix, compensates for the heat leak, or provides cooling power.

Up to 1K the quasi-classical nature of ^{3}He is apparent, but it still resembles ^{4}He in everything besides mass and vapor pressure. However, on the order of 0.1K, the quantum nature governed by Fermi Dirac statistics becomes extremely apparent. The pure ^{3}He sample is cooled by heat step exchangers and the refrigerator. After this stage the cooled ^{3}He is sent into the sample chambers.

D. Nuclear Demagnetization

The final step in the cooling process is the adiabatic demagnetization of Copper and Praesodymium nuclei. These nuclei have been spin polarized by contact with the dilution refrigerator and being placed in a strong magnetic field on the order of 7.5 T. They are cooled using a dilution refrigerator to about 7 mK. This causes the spin entropy to be reduced significantly as the spins increasingly populate the lowest energy states. When the demagnetization stage is isolated thermally, the entropy stays constant save for the effects of a heat leak. Thus, the temperature of the stage can be varied by raising or lowering the magnetic field.

A metal sinter is connected to one of the two sample chambers. The result is a thermocoupling between the nuclear cooling stage and one chamber of the experimental apparatus. This experimental apparatus can be seen in Figure 3. The two sample chambers are filled with pure ^{3}He, so cooling the metallic nuclei and the connected sinter also cools the ^{3}He. In this way the temperature of our ^{3}He could be varied to observe transitions within the ^{3}He with extremely small heat currents. This technique is usable for roughly a month: due to stray heat leaks it must be regenerated and can't be run as a truly continuous process.
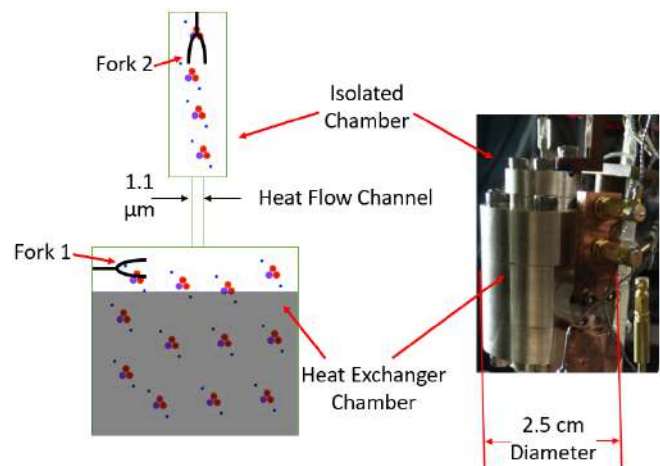

FIG. 3. The heat exchange and isolated chambers. In each of these chambers there are quartz tuning forks. The chambers are connected via a small channel where confinement occurs. The isolated chamber has a volume of 0.14 cc, the heat exchange chamber has a volume of 1.5 cc.

IV. EXPERIMENTAL METHODS

In the experimental space there was a heat exchange chamber, and an isolated chamber. In each of the chambers there was a quartz tuning fork. The quartz tuning forks were driven via an AC current. From these forks the frequency and Q factor were recorded. The Q factor

is defined as:

$$Q \stackrel{def}{=} \frac{f_r}{\Delta f} \qquad (1)$$

Where f_r is the resonant frequency and Δf is calculated from the full width half max of a measured distribution, and then related to frequency. The resonant frequency is measured from the input signal or alternating current. Δf is calculated from the resulting power loss of the forks as they oscillate in the liquid. This power loss relates to the frequency distribution of the forks oscillation.

A transition in ^{3}He corresponds to sharp changes in both frequency and Q. By measuring Q, we were able to identify both superfluid to normal state transitions. The second order normal to superfluid transition is accompanied by a discontinuity in the slope of Q factor versus temperature. The first order transition between A and B phase corresponds to a discontinuity of Q factor versus temperature. Measuring Q factor and frequency also allowed us to calculate the temperature of the superfluid in the isolated chamber, even though it was weakly thermally coupled from the melting curve thermometer.

A. Challenges of Low Temperature Thermometry

Here we will justify the use of a quartz tuning fork to indirectly measure temperature rather than a more traditional thermometer. One of the biggest challenges to low temperature thermometry is the necessity of calibration points within the system. At temperatures below 4.2 K only helium remains in the liquid phase. At 2.17 K ^{4}He undergoes its lowest known transition to a superfluid. As a result, only ^{3}He provides phase transition points for calibration before this point.

A common measurement technique for temperature is a resistor with a known function of resistance to temperature. For example thermocouples with differing metal conductors could have been used. These leads could be connected to the point of interest. The problem with this method is that at the thermometer power decreases rapidly at low temperature.

A capacitor may be used for temperatures below the superconducting transition point. A capacitor could measure the pressure of a gas or liquid by correlating it to the bowing of a thin plate. Then, the pressure may be measured and correlated to a temperature. This works because vapor pressure is closely related to the temperature of a substance. Alternatively, the capacitance of a liquid filled space may be measured. The density of the liquid may then be transduced because the atoms will have a dielectric constant. More atoms between the capacitors causes a greater dielectric contribution, or a higher capacitance. Unfortunately, this is a weak thermometer and is not usable in temperature regimes of interest here. A resistor could be used until its superconducting transition, then one could switch to a parallel plate capacitor and measure vapor pressure. The problem with this is that the resistor and capacitor duo would still need to be supplemented by an instrument that could directly provide the state of the substance being measured. Another problem is the thermal coupling of the thermometer to the liquid ^{3}He. The thermometer would have to remain in constant equilibrium with the system in order to give accurate temperature.

B. Justification for a Quartz Tuning Fork

Many of these problems are avoided entirely if we instead use a quartz tuning fork to measure the viscosity of the substance. In both liquid and superfluid ^{3}He viscosity is directly correlated by temperature in well characterized ways. Therefore, using the Q factor to infer the viscosity, we may calculate the temperature of the ^{3}He. This removes the challenge of thermal coupling because a quartz tuning fork relies only on inertial and viscosity mediated interactions. The exact process for calculating temperature is expanded on in the data analysis section.

Yet another benefit of the quartz tuning fork is discontinuities and jumps in the Q factor and frequency correspond with the first and second order phase transitions of ^{3}He at low temperatures. This creates the calibration points necessary to correlate the Q factor to temperature.

V. DATA COLLECTION

Two modes of data collection were employed to gather statistics. Both essentially changed the temperature at constant pressure. These two methods were: slow temperature change ramps through transition points, and overdriving the quartz tuning forks to create pulses of heat.

A. Nuclear Magnetization Controlled Temperature Ramps

The first method, slow cooling or warming ramps, was done with adiabatic demagnetization. The theory behind this was discussed earlier in the experimental set up section. A magnetic field can be decreased slowly to offset a heat leak, or quicker to cool the fluid. Conversely, a magnetic field may also be increased to heat the fluid. Heating and cooling ramps were often at rate of about 0.01 mK/hr. This method provides precise control over temperature and was used to identify the superfluid transition as well as the A-B transition. The benefits of this method include minimizing the heat current between chambers. This allowed for a closer observation of the mechanisms causing the phase transition. Having a high heat current runs the risk of initiating the process that causes B phase nucleation. Moreover, the slow temperature ramps allow for more accurate temperature measurments of points exactly where the transitions were

occurring. A slower temperature ramp directly translates to a higher resolution of points for each transition. From this form of data collection, statistics on the phase transitions of ^{3}He were recorded.

B. Overdriving the Quartz Tuning Forks

The second method, overdriving the tuning forks, was done by greatly increasing the AC amplitude driving their oscillation. This was usually done for about 100 seconds, although the time varied up to 300 seconds for very low temperatures. Overdriving caused them to vibrate at much larger amplitude, adding mechanical heat to the system. This provided two interesting pieces of data. The increase the temperature allowed us to observe phase transitions in the presence of a high heat current during the thermal re-equilibration, while perturbing the fluid allowed us to observe the relaxation time of the fluid.

In experiments discussed here, the fork in the isolated chamber was overdriven, bringing the fluid above the normal to superfluid transition point. The fluid was then allowed to cool back into equilibrium. This allowed us the chance to observe both the superfluid transition, as well as the AB transition. From this, the relaxation time of the fluid as well as the temperature at which the AB transition occurred were recorded.

VI. DATA ANALYSIS

Python and Matlab were used for data treatment. Python was used for fitting and treating data obtained from slow temperature ramps. Matlab was used for fitting the data gathered while pulsing and for determining the relaxation time.

A. Temperature Ramp Analysis

Data collected at a particular pressure was imported and treated using a class structure. The class structure allowed us to create a program that could uniformly treat all the data with the same operations and assign important statistics of the run as attributes to the class. The data was cut to only work with one monotonically changing temperature ramp at a time. The temperature recorded from the melting curve thermometer was then fit with a low order polynomial. Pressure was input and converted into a known superfluid transition temperature using data from Greywall [3]. This temperature is consistent for a known pressure. As a result, when the superfluid transition point was identified in the heat exchange chamber, we may account for the offset of the melting curve temperature to read this. This can be seen in Figure 4.

Because fork 1 is in the heat exchange chamber, the melting curve thermometer gives temperature readings that are close to the true temperature of the fork, aside from a small thermal lag. Using the superfluid transition point, we can find the temperature of the melting curve at that time, and shift it up or down to match the temperature given by Greywalls formula. This shift comes in the form of a small correction to the constant term in our temperature fit. It is usually on the order of 0.01 mK. Even though the heat exchange chamber is thermally coupled to the point the melting curve thermometer reads temperature, this offset may have been caused by a small thermal lag. Due to this adjustment, the temperature fit may be used for the temperature near fork 1.
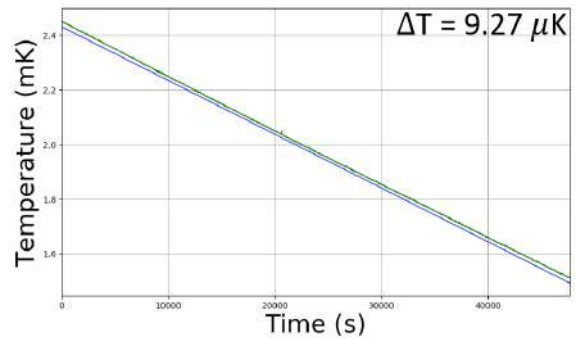

FIG. 4. Temperature of the Melting Curve Thermometer (Green) and Temperature of our fit (Blue) after shifting temperatures to the correct normal phase to superfluid transition point.

In ^{3}He the viscosity changes with temperature [1]. In dampened harmonic oscillators in a fluid, the Q factor also changes with viscosity. Therefore, given that we know the temperature of fork 1 and its Q factor, we may correlate the two. Thus, we can fit fork 1's Q as a function of time. We can then correlate Fork 1's Q factors to the corrected and fitted temperature for the same time.

We fit Q to time with a high order polynomial and a step function of the following form:

$$Q(t) = \sum_{n=0}^{N} a_n * t^n + b * u(t - t_{AB}) \qquad (2)$$

Where b is the magnitude of the discontinuous jump in Q factor at the A to B transition, and t_{AB} is the time of the jump. Using a step function along with a polynomial fit allows us to account for the first order phase transition without wasting time on an extremely high polynomial fit. This is shown in Figure 5.

Furthermore, we can use the Q factor in fork 2 to identify the superfluid transition point within this fork. Like in fork 1, the measured Q factor is related to the temperature at that time. As a result, we were able to correlate the temperature at this point to the superfluid transition point in fork 1. Using that point as a start, we applied a nearest neighbor closest point search via a binary sort.
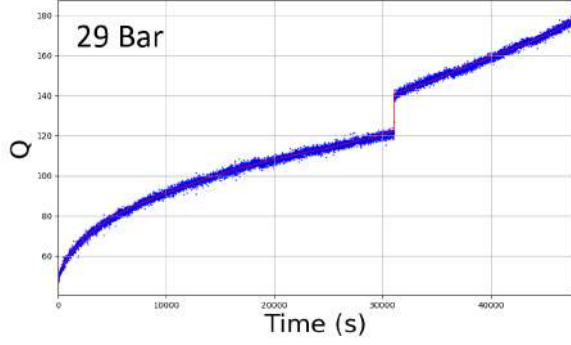
FIG. 5. The Q factor of Fork 1 being fit with a high order polynomial and a step function. In this specific example, the polynomial is a 7th order polynomial.

Using this, we mapped each point in fork 2 to a point in fork 1 in Q space. The correlation between Q and temperature meant that we could then correlate the points in fork 2 to temperatures at points with similar Q factors in fork 1. As a result, we could find the temperature of A to B transitions in both bulk and in isolation.
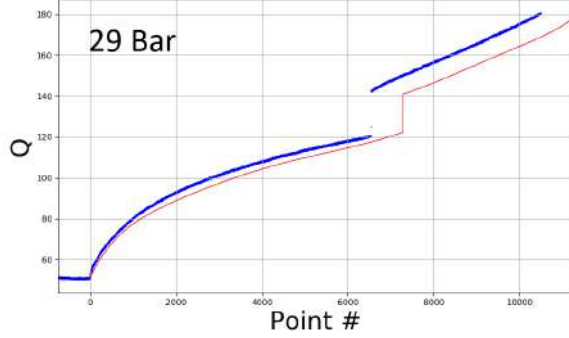

FIG. 6. The fit of Fork 1 overlaid on the Q factor from Fork 2. The points of the normal to superfluid transition were shifted to match so that the k-NN Search could be applied. Notice point number was used for the search instead of time, this was to help use a consistent indexing of the data when searching..

This allowed us to identify transition points in pressure-temperature space and relate them to the phase diagram of ^{3}He.

B. Pulsing Data

The pulsing data was treated in Matlab. The data was cut so that the temperature was monotonically increasing or decreasing. This allowed for the pulses to be indexed, and the temperature to be fit with a low order polynomial. When looking at Q over time, pulses in superfluid were inverted compared to pulses in the normal state. This can be seen in Figure 7.

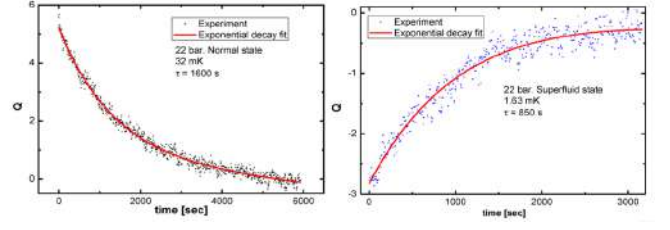The background would be removed using a polynomial fit of points just before the pulse was launched. These

FIG. 7. Fits of pulses in both the superfluid and normal state of ^{3}He. The pulses are inverted because Q increases with rising temperature in the normal state due to lower viscocity, while it decreases with rising temperature in the superfluid.

pulses would have a median filter applied to them to reduce the noise. After this filter, an exponential fit would be applied. The fit would be in the form:

$$Q(t) = B + A_0 * exp(\frac{-t + t_0}{\tau}) \qquad (3)$$

This was used to estimate the parameters B, A_0, t_0, and τ. Then, a small linear time dependent term was used to further reduce error as it appears from removing the background. In this second fit, the parameters from the first fit were used as guesses for the second fit. The second fit came in the form:

$$Q(t) = B + K * t + A_0 * exp(\frac{-t + t_0}{\tau}) \qquad (4)$$

Where K is a correction to the background removal in the form of a linear slope. From this we recorded the relaxation time, τ.

VII. RESULTS

Statistics were gathered on the transition points within the bulk heat exchange chamber, as well as within the isolated chamber. The timing and temperature at which these transitions occurred were recorded. Collecting the timing gave us insight into which chamber was nucleating the A-B transition first. While the temperature at which the phase transition occurred helped us understand when supercooling occurred, and what conditions made the A or B phase more favorable in confinement. The points can be seen overlaid on the ^{3}He Phase Diagram in Figure 8.

The A to B Transition in cooling occurred first in time in the Heat Exchange Chamber for intermediate pressures, at both 25 bar and 22 bar. However, at the highest pressure of 29 bar, the transition in both chambers was observed to occur at the same time. For lower pressures below the poly critical point, A to B transitions were only observed in the isolated chamber, and no B to A transitions were observed in heating.

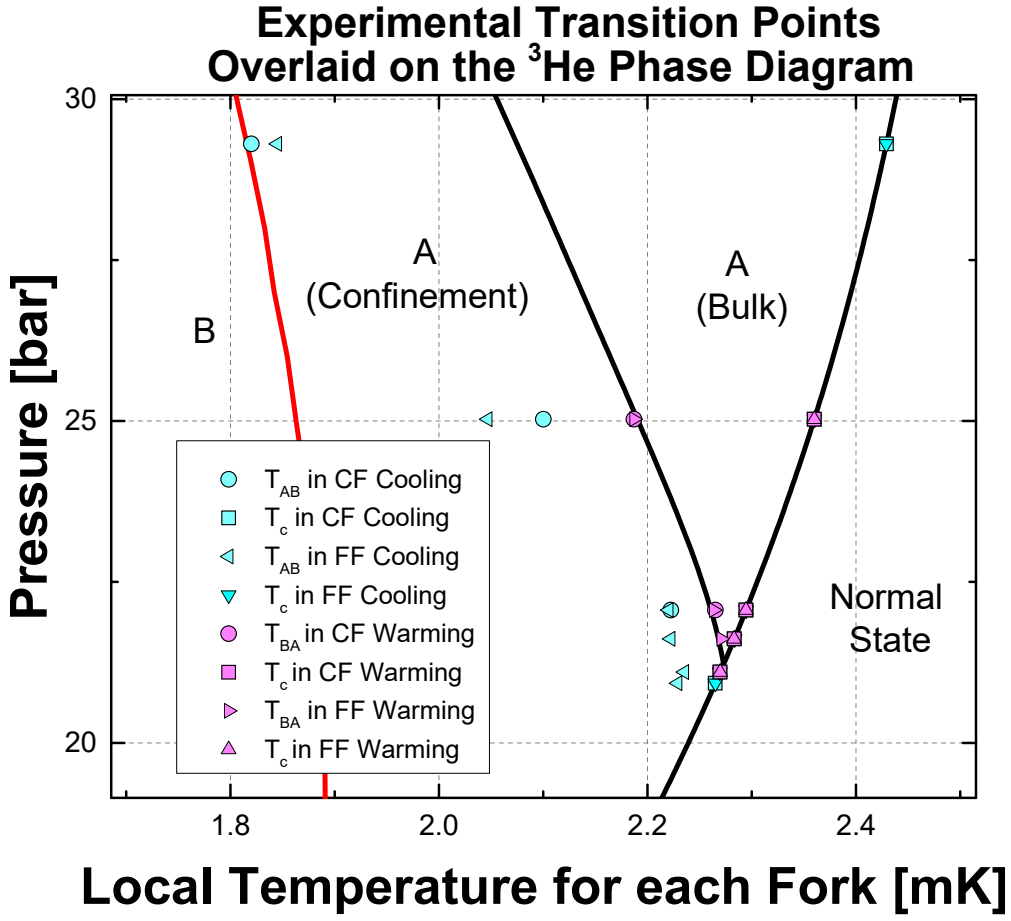During pulsing, the relaxation time of the superfluid and normal state were measured. The measured τ in

FIG. 8. Experimental transition points overlaid on the ^{3}He phase diagram within the region of interest surrounding the poly critical point. HE stands for the heat exchanger chamber. IC stands for the isolated chamber.

normal state is shown in Figure 9, on the left. The relaxation time was measured across a large temperature range. The τ was compared to the expected relxation time calculated using Greywalls thermal conductivity and heat capacity data [3]. The thermal resistance was also calculated using τ and the heat capacity. The thermal resistance is equal to relaxation time divided by the heat capacity. This resistance is shown in Figure 9, on the right. Low temperature behavior of relaxation time is expected to scale with T^2, but instead shows scaling with T. This is not explained here, but we hypothesize that it is possibly due to the confined geometry. The thermal transport mean free path exceeds the separation of the parallel plates at both zero bar and 22 bar.

VIII.   DISCUSSION

At the highest pressure, the two chambers underwent the A to B phase transition at the same time. This suggests one of two results. The first is that the nucleation

was occurring in the 1.1 μm channel and nucleating both the heat exchange chamber and the isolated chamber at the same time. The second is that the transition occurred in the heat exchange chamber below the A-B transition point within confinement. This may have then nucleated the channel, which would in turn cause the A to B transition in the isolated chamber. This entire process would happen quickly enough that it would appear instantaneous to our measurement equipment. This can be seen in Figure 10a.

However, at intermediate pressures the heat exchange chamber underwent the A to B transition earlier in time, seen in Figure 10b. This might be expected, because in cooling the heat exchange chamber will reach lower temperatures first. However, the A to B transition occurred at different local temperatures for both channels. This suggests that the heat exchange chamber underwent the A to B transition, then sometime later the isolated chamber underwent a separate A to B transition. This suggests that a different mechanism was causing the nucleation of the B phase here compared to high pressures.
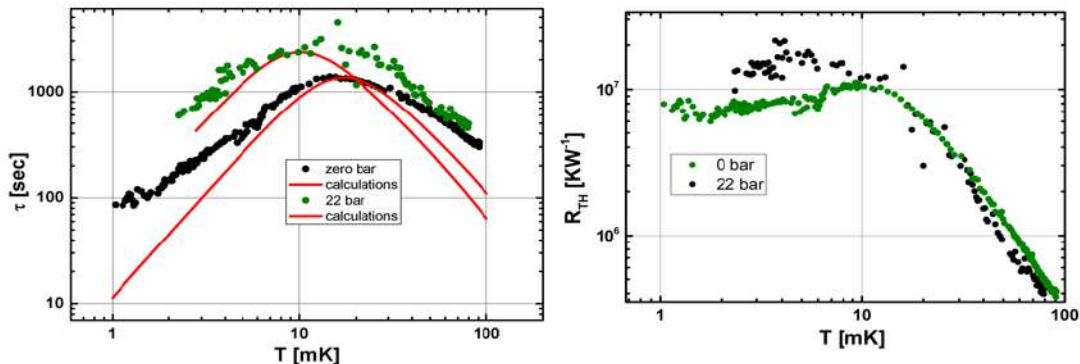
FIG. 9. Relaxation time (left, directly measured) and thermal resistance (right, calculated using data from the Greywall text [3]) .
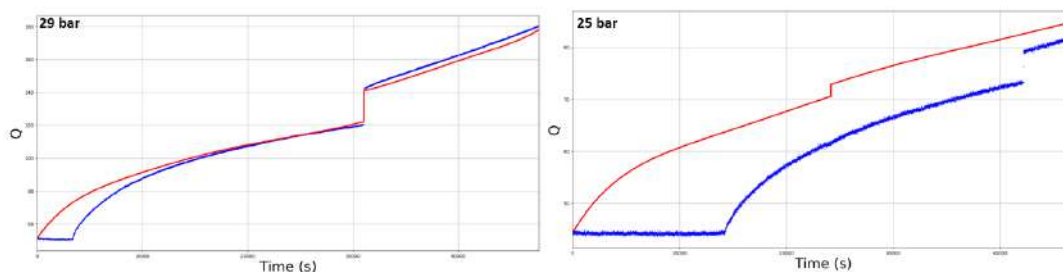

FIG. 10. Q factor over time for both forks at two different pressures. Note that 29 bar shows the transition happening simultaneously while the 25 bar shows the transitioning happening first in the heat exchange chamber.

We see the B phase nucleation occur first in time in the heat exchange chamber, but still at lower temperatures than predicted by the phase diagram of ^{3}He. The fact that the heat exchange chamber is undergoing its A to B transition first suggests that supercooling is less energetically favorable than in the isolated chamber. This is likely due to the presence of the sinter, this presents a diversity of sites where the B phase may be nucleated first. A short time later, we see fork 2 show signs that the isolated chamber has undergone its own A to B transition. The fact that the supercooling of the A phase continues longer in the isolated chamber suggests that it has less sites on its surface to promote the B phase and disrupt the supercooling.

At pressures below the poly critical point, we no longer see the A phase in the heat exchange chamber. Since there is no magnetic field, the A phase should not be nucleated in the bulk below the poly critical point. Because there is no observed A phase in the heat exchange chamber, we can conclude that there is no stray magnetic field on the experiment cell. We continue to observe the A to B transition in the isolated chamber, further demonstrating the supercooling of phases within the isolated chamber. The appearance of the supercooled A phase below the poly critical point can only be due to the present of the A phase in the channel. Rather than creating the energetically preferred B phase, the fluid follows a path where

the interfacial energy between the confined ^{3}He and the bulk ^{3}He in the isolated chamber is minimized by seeding the A phase into the isolated chamber. Thus, the A phase observed below the poly critical point is solely present due to interfacial physics. On warming only the B phase is observed until the critical temperature in the isolated chamber.

On warming, we see slight time differences between the heat exchange chamber's and the isolated chamber's B to A transition. However, upon accounting for offsets, the B to A transition occurs at the thermodynamically appropriate temperature. Thus, it is apparent there is no superheating of the B to A transition. This is likely because the A phase at a minimum is present in the channel and can seed the B to A transition when it is the preferred phase.

IX. CONCLUSION

While results presented here indicate new mechanisms may be responsible for the A to B phase transition, these mechanisms are not yet well characterized. In the future, experiments will aim to characterize these mechanisms and learn more about the effects of confinement on ^{3}He.

Experiments will also be done to further explore the high pressure regime and learn more about the effects

occurring there. The energetically favored phase in the channel and exploration of supercooling in the channel is particularly interesting. Regions of pressure below the poly critical point will also need to be explored. In these regions super cooling is observed in the isolated chamber but not in the heat exchange chamber. Studying this region will provide further insight into the mechanism causing nucleation of the B phase in the A phase.

---

[1] Dobbs. *Helium Three.* Oxford University Press, 2000.

[2] Lounasma. *Experimental Principles and Methods Below 1K.* London and New York: Academic Press, 1974.

[3] D. Greywall, Page 33, **Volume 33, Number 11**, Physical Review B, 1986.

[4] Phase is a bulk property of a substance, at temperatures very near to absolute zero single atoms or particles are usually being manipulated or measured. As a result, describing the phase of an element at pico-Kelvin temperatures is a rather abstract thing to do. However, at temperatures in the mili-Kelvin or even micro-Kelvin scale helium is the only fluid element.

[5] S-wave pairing refers to the common naming convention of the angular momentum of electrons in orbital shells. The s-wave pairing refers to the first state that has no angular momentum, and therefore only one possible projection onto the z-axis. Non-s-wave pairing implies that the state of zero angular momentum does not exist as an outcome of this interaction.

[6] Transfer occurred every 3 to 4 days throughout the duration of this experiment.

[7] Kelvin drag refers to the interactions of ^{3}He particles and the ^{4}He superfluid caused by the inertia of the ^{4}He particles. It is not the same as a viscosity of the liquid, which is effectively nonexistent because ^{4}He is in its superfluid state here.

Optimizing Pulse-Echo Ultrasound Instrumentation Using Two-Dimensional Computational Modeling

Jiatian Wu[1], Sayak Ghosh[2], and Brad Ramshaw[2]

[1]Department of Physics, Emory University, Atlanta, GA 30322
[2]Department of Applied and Engineering Physics, Cornell University, Ithaca, NY 14853

Abstract— An unique pulse-echo ultrasound technique is developed to measure the speed of sound in condensed matters and helps identify the second-order phase transitions of the matters. On the one hand, ultrasound measurement is advantageous for its simplicity and efficiency compared to other thermodynamics measurements. The current apparatus setup is sensitive to detect subtle changes of vibrations due to its use of high-frequency sound waves. On the other hand, its sensitivity occasionally leads to wave interference in the results for some unknown reason. Thus, a computational model is built to simulate the wave propagations of a sample in the apparatus in order to find out the potential factors affecting the wave propagations and be able to optimize the design for future sound velocity measurements in numerous materials.

I. INTRODUCTION

The thermodynamic properties of condensed matters, such as superconductors and heavy fermion compounds, have some peculiar behaviors regarding to their phase transitions, including heat capacity $C_p = -T\partial^2 F/\partial^2 T$, magnetic susceptibility $\chi = T\partial^2 F/\partial H^2$, and elastic modulus $c_{ij} = \partial^2 F/\partial \epsilon_i \partial \epsilon_j$ [3]. In the macroscopic view, these properties are the second order derivatives of the free energy F with respect to temperature and become discontinuous at the point of a critical temperature T_c. In the microscopic view, the electronic structure of a material changes during its phase transition and result in breaking the original symmetry of the system[5].

While the phase transitions of conventional materials are usually simple for being the first order derivative of the Gibbs free energy, examples like the transformation of ice from water, the second-order phase transitions have much more interesting physical properties and complex structures in condensed matters. Some well-known second-order phases are like superconductivity and magnetism. For example, when iron reaches a curie temperature $1034K$, its magnetization changes drastically and it becomes paramagnetic. Thus, thermodynamics plays an important role in todays condensed matter research as it is an efficient way to find phase transitions. Studying thermodynamics of a range of different materials helps us categorize their phases and possibly identify the "hidden order" phase of materials.

Elastic modulus is one of the thermodynamic properties that our lab adopts to find the phase transitions of materials. It is a coefficient that describes how a material is being deformed elastically by the force. In a mathematics sense, the elastic modulus c_{ij} is the curvature of the free energy

with respect to strain ϵ. However, the elastic modulus is not easy to be measured directly. Instead, we measure the speed of sound v traveling in the material, because elastic modulus c_{ij} is correlated to the speed of sound as $v = \sqrt{c_{ij}/\rho}$, where ρ is the material density.

Our lab uses a pulse-echo ultrasound technique which applies the high-frequency sound waves through a piezo-electric transducer to a testing sample to probe the speed of sound of the material. The technique was first developed by Suslov et al. to measure the speed of sound of a material and its attenuation as a function of a external variable, like temperature or magnetic field [7]. Our group modifies the technique so that it can both eliminate large fraction of electrons and allow digital post-processing [4]. Since phase transitions often happen abruptly, ultrasound measurement has its advantages in tracking even the subtle change of phase compared to other thermodynamics measurements. The technique is also efficient in collecting data because the whole measurement usually takes place in tens of microsecond or hundreds of nanosecond.

However, when we tested the samples using the ultrasound technique in the previous work, some wave interference happened occasionally and prevented us from measuring the accurate attenuation of the material. To better understand the cause of the interference and be able to reduce it, a computational simulation of the instrumentation is needed to probe the wave propagation in the sample.

II. METHODS

A. *Pulse-Echo Ultrasound Instrumentation*

The instrumentation was set up as shown in Fig. 1 below. By applying a short burst of electronic signals on a piezo-electric transducer, the signals were converted from electrical signals to sound waves and transmitted through a crystal sample. The waves traveled back were received by the same transducer and created an "echo train" in the plot (see Fig.3). As the waves propagated in the sample, we could measure the absolute phase ϕ, the distance between the "echo trains" and hence calculate the absolute speed of sound v, $v = 2\pi f l/\phi$, where f is the frequency we apply to the transducer, and l is twice the sample length. The phase transition happens instantaneously and hence is easy to miss if the measurement is not precise enough. To further improve the precision, we measured the phase velocity of the pulse waves instead of
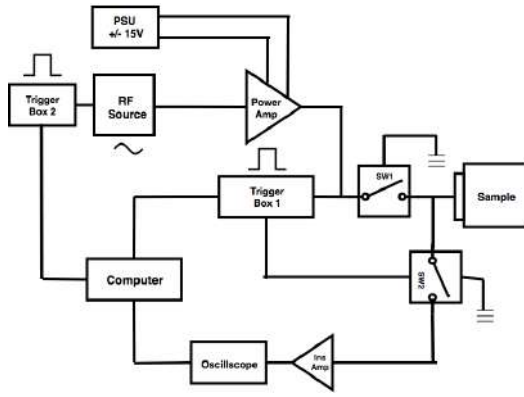
Fig. 1: Schematic representation of the ultrasound instrumentation. The instrumentation has a complete power supply and filter system. The program LabVIEW first sends out a short burst of electronic signals to trigger box 1 [Tektronix AFG1062] to generate square-pulse signals. A trigger box controls a switch(SW) [ZFSWHA-1-20+]. At the same time, a radio-frequency(rf) source [Agilent 83650B] generates continuous microwaves and the waves are amplified by a power amplifier [Mini-Circuits® 15542] with the $15V$ power supply(PSU) [BK Precision 1672]. The two signals combine together to create a mix of standing waves. The waves travel back and forth through a sample and send back as electrical signals. The signals are amplified by a instrumentation amplifier [MITEQ]. The signals are received by a oscilloscope [Tektronix MDO3104] and processed by the computer.

its group velocity. We calculated the change of the speed of sound, Δv,

$$\Delta v = -2\pi f l \frac{\Delta \phi}{\phi^2},$$

where $\Delta \phi$ is the phase shift of the sound waves in an echo. The sample was placed in a low-temperature environment and its change in speed of sound was recorded by lowering the temperature. We would also need to know the fundamental frequency of the transducer since the transducer is excited when the harmonic resonances are applied.

The technique was different from Suslovs setup as it could record the positions of each microwave inside an "echo train" instead of estimating the positions of all waves by averaging. Having more data points improved the accuracy of attenuation of the sample as it could now calculate the exponential decay function by data fitting and get the loss factor Γ.

B. Computational Model

A finite-element analysis program COMSOL Multiphysics was used to simulate the wave propagations in a crystal sample on the top of a piezoelectric transducer to find out the cause of the wave inference. The built-in package Piezoelectric Device module included both Structural Mechanics and Electric Potential modules and therefore was used for the simulation. The simulation was solved deliberately as a

two-dimensional problem for its significantly smaller computational cost. A pulse-echo electric potential was applied on a side of the transducer to simulate the processed signals sent from the instrumentation. The governing differential equation for the linear elastic material is given to solve for the material's displacement field $\vec{u}$,

$$\rho \frac{\partial^2 \vec{u}}{\partial t^2} = \nabla \cdot s + \vec{F}v,$$

where ρ is the density, and s is stress.

The material we chose was Tungsten for the crystal sample for its high density and lithium niobate($LiNbO_3$) for the transducer for its common use in the lab (see Table 1 for parameter values). The boundary conditions of the sample were suppose to be free on all four sides but instead set to be low-reflective on the left and right sides to reduce the wave reflection distractions (see Fig.2a). The damping coefficients of both the sample and transducer were taken from the literatures [1] if possible and, otherwise, estimated to match with the experiment results (see Table 2). In consideration of damping effects, eq.2 is modified to be as

$$\rho \frac{\partial^2 \vec{u}}{\partial t^2} + \alpha_{dM}\rho \frac{\partial \vec{u}}{\partial t} = \nabla \cdot (s + \beta_{dk}\frac{\partial S}{\partial t}) + \vec{F}v,$$

where α_{dM} is the mass damping parameter for the sample and β_{dK} is the stiffness damping parameter for the transducer. Mesh was also taken care due to the short time duration of the high-frequency pulse.

TABLE I: Mechanical and electrostatic properties of the materials used in the COMSOL model

Material Name	Tungsten	Lithium Niobate	"Half" Tungsten *
Density (kg/m^3)	17800	4700	8900
Young's modulus (Pa)	3.6e11	N/A	1.8e11
Poisson's ratio	0.28	N/A	0.14

* "Half" Tungsten is used later for adding an extra layer in between the sample and the transducer.

A time-domain study was taken in each simulation, and the time step was determined by obtaining at least five or more degree of freedom within the wavelength of ultrasound λ[2]. We then took a frequency-domain study to test the resonances of the transducer. Parametric Sweep was implemented in the time domain study to verify the results.

Several aspects of the sample were tested to see how the change would affect the wave propagation in it and thereby optimize the design, including increasing the roughness of the sample surfaces, finding the better sample width, and adding an extra layer between the sample and the transducer.

The roughness of a surface can be described by the composition of many elementary waves and the spatial frequency of the surface oscillations (see Fig. 2b). According to Sjodin, surface roughness can be quantified as follows,

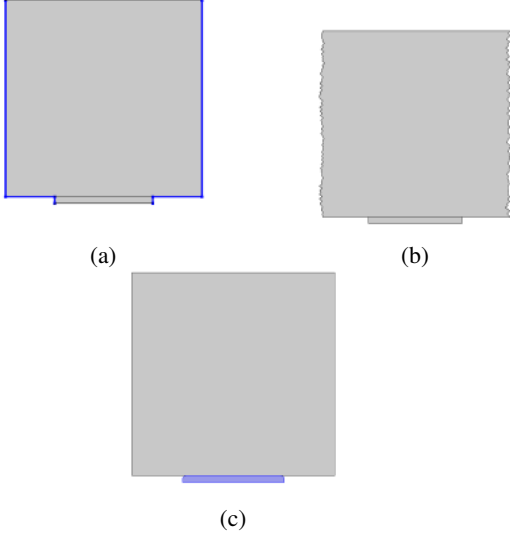$$f(x) = \sum_{m=-M}^{M} a(m)\cos(2\pi(mx) + \phi(m)),$$

(a)   (b)

(c)

Fig. 2: (a) Low-reflective boundary conditions. (b) Adding fillets on the edges. (c) Increasing the surface roughness of the sample.

where x are spatial coordinate, and m are spatial frequency [6]. By increasing both the amplitude and spatial frequency, we studied the effect of surface roughness on wave propagations. Sample size and wave interference were studied as well.

TABLE II: Parameters used by default.

Variable	Value (unit)	Description
f	5 (MHz)	Frequency
N	50	Spatial frequency resolution
b	0.5	Spectral exponent
W_t	3 (mm)	Transducer width
H_t	0.2 (mm)	Transducer height
W_s	6 (mm)	Sample width
H_s	6 (mm)	Sample height
β_{dk1}	2e-10 (s)	Sample stiffness damping
β_{dk2}	2e-7 (s)	Transducer stiffness damping parameter

$*$ Some parameters values change in the simulation for testing purpose.

III. RESULTS

The default simulation has a $6mm \times 6mm$ sample and a $3mm \times 0.2mm$ piezoelectric transducer. The wave function is $\sin(2\pi ft)$, where f is $5MHz$ and t is $2.5e-5$ seconds in $3e-9$ time step. The results shows the ideal situation if no wave interference occurs (see Fig.3).

The same setting is applied to a frequency domain study, and we get the following harmonic resonances of the transducer (see Fig.4). The resonance happens at around the expected frequency value where the transducer length is a multiple of half of its corresponding wavelength, $L = n(\lambda/2)$. Wavelength λ can be calculated as $\lambda = v/f$, where v is the speed of sound in the material.
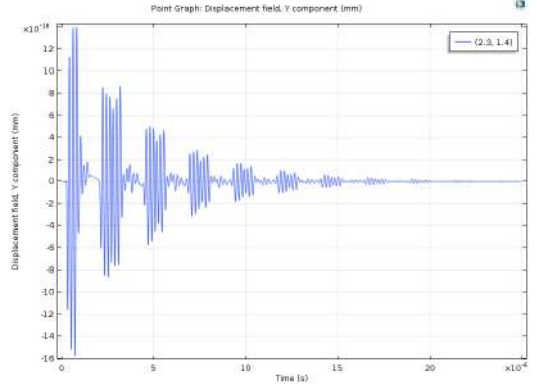

Fig. 3: The wave propagation in the sample. The electric signals turn into sound waves and traverse in the sample with no wave interference. The displacement of a point (2.3,1.4) is plotted as a function of time.
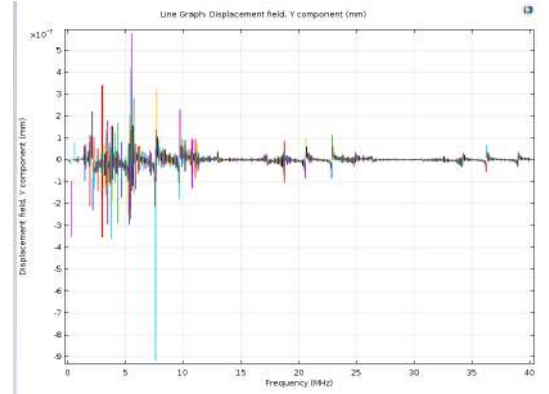

Fig. 4: The resonance of the transducer in a frequency domain when the transducer is 1mm. The simulated resonances happened around 6.68, 20.6, 34.4 MHz, as calculated.

A. Size

We defined relative width W_r as the ratio of the transducer and the crystal sample, $W_r = W_{transducer}/W_{sample}$ and tested different transducer widths in a $4mm times 4mm$ sample. The relative width is critical to the wave propagation, as neither being too wide or too narrow helps reduce the wave interference. When the relative width was larger than 3/4, the wave fronts were too wide and quickly hit the sample boundaries before reaching to the other side; when the relative width was smaller than 1/8, the edges of the transducer were too close to each other and generated relatively large wave interference. The relative width around 1/4 had the minimized wave interference (see Fig.5). Adding fillets on the corners of the transducer also helped reduce the interference greatly, as expected (see Fig. 2c).

B. Surface Roughness

The surface roughness helped noise reduction in some degree when the waves echo back for three times or more, depending on the wave frequency. In order for the roughness to take effect, the spatial wavelength of the surface roughness
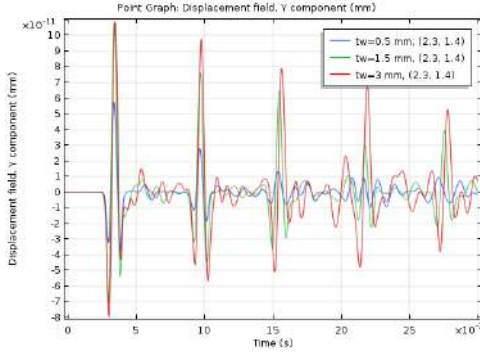
Fig. 5: The wave propagations in the sample when the width of the transducer varies.
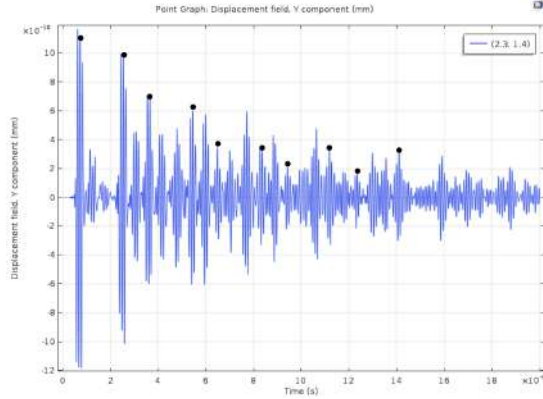

Fig. 6: The wave propagation in the sample when an extra layer of 1.25mm thickness is added in between. Knowing the relative speed of sound, we can distinguish when the sound wave reaches to the point (2.3, 1.4), and they are marked in black dots in the figure. The sixth and eighth wave echoes have a smaller amplitude than the seventh and ninth echoes, which is caused by the wave interference. When the wave travels through the added layer, it allows the layer to vibrate and generate additional waves. The two waves have a phase difference, and they combine in the sample, creating constructive and destructive interferences shown in the plot.

should be approximately equal to or smaller than the order of magnitude of the sound wave, which was tens of micrometers if a $50 MHz$ sound wave was applied.

C. Wave Interference

A layer was added in between the sample and the transducer to simulate the potential interference of the glue that is used to attach the two parts together in the experiment. An observation was found as the thickness of the layer increased. When the thickness of the layer was an odd multiple of the quarter sound wavelength $\frac{n}{4}\lambda (n = 1, 3, 5, ...)$, the wave propagation showed similar wave patterns where the superpositions of the waves occurred at the same positions. Such wave interference would intervene the wave amplitude measurement and hence lead to a wrong value of the loss factor Γ(see Fig.6).

IV. CONCLUSION

The work was done to show that the wave interference in the previous experiments may cause by the excessive amount of glue between the sample and transducer. Since the experiment runs in micrometer-scaled system, it is not an easy task to reduce the glue thickness to be insignificant compared to the rest of the setup. Further optimization is needed to find a thickness that can generate in-phase waves to avoid the wave interference. Further work can be done to find the quantitative correlation between the wave frequency and surface roughness of sample materials to minimize the noise.

REFERENCES

[1] I Chowdhury and S Dasgupta. Computation of rayleigh damping coefficients for large systems. 2003.
[2] W Frei. Simulation tools for solving wave electromagnetics problems. 06 2015.
[3] K Modic, Maja D. Bachmann, Brad Ramshaw, Frank Arnold, Kent Shirer, Amelia Estry, Jon Betts, Nirmal Ghimire, E D. Bauer, Marcus Schmidt, M Baenitz, Eteri Svanidze, Ross Mcdonald, Arkady Shekhter, and Philip J. W. Moll. Resonant torsion magnetometry in anisotropic quantum materials. 02 2018.
[4] Brad Ramshaw, K Modic, Arkady Shekhter, Philip J. W. Moll, M K. Chan, Jon Betts, Fedor Balakirev, A Migliori, Nirmal Ghimire, E D. Bauer, F Ronning, and Ross Mcdonald. Annihilation of weyl nodes in the extreme quantum limit of taas. 04 2017.
[5] J. P. Sethna. Order Parameters, Broken Symmetry, and Topology. *eprint arXiv:cond-mat/9204009*, April 1992.
[6] B. Sjodin. How to generate random surfaces in comsol multiphysics®. 2017.
[7] A. Suslov, Bimal K. Sarma, J. Feller, and J. Ketterson. Ultrasonic instrumentation for measurements in high magnetic fields. i. continuous magnetic fields. *Review of Scientific Instruments*, 77(3):035104, 2006.